DISSERTATIONES
CHIMICAE
UNIVERSITATIS
TARTUENSIS
197

MEELIS HÄRMAS

Impact of activated carbon microstructure and porosity on electrochemical performance of electrical double-layer capacitors

DISSERTATIONES CHIMICAE UNIVERSITATIS TARTUENSIS
197

DISSERTATIONES CHIMICAE UNIVERSITATIS TARTUENSIS
197

MEELIS HÄRMAS

Impact of activated carbon microstructure and porosity on electrochemical performance of electrical double-layer capacitors

UNIVERSITY OF TARTU
Press

Institute of Chemistry, Faculty of Science and Technology, University of Tartu, Estonia

The dissertation is accepted for the commencement of the degree of Doctor of Philosophy in Chemistry on June 12th, 2020, by the Council of Institute of Chemistry, University of Tartu.

Supervisors: Senior Research Fellow Alar Jänes, Ph.D.
University of Tartu, Estonia

Senior Research Fellow Thomas Thomberg, Ph.D.
University of Tartu, Estonia

Opponent: Assistant professor Olivier Crosnier, Ph.D.
University of Nantes, France

Commencement: 26.08.2020 at 14:15. Auditorium 1020, Ravila 14a, Tartu

ISSN 1406-0299
ISBN 978-9949-03-424-6 (print)
ISBN 978-9949-03-425-3 (pdf)

Copyright: Meelis Härmas, 2020

University of Tartu Press
www.tyk.ee

CONTENTS

1. LIST OF ORIGINAL PUBLICATIONS

I. **M. Härmas**, T. Thomberg, H. Kurig, T. Romann, A. Jänes, E. Lust, Microporous–mesoporous carbons for energy storage synthesized by activation of carbonaceous material by zinc chloride, potassium hydroxide or mixture of them, J. Power Sources. 326 (2016) 624–634.

II. **M. Härmas**, T. Thomberg, T. Romann, A. Jänes, E. Lust, Carbon for Energy Storage Derived from Granulated White Sugar by Hydrothermal Carbonization and Subsequent Zinc Chloride Activation, J. Electrochem. Soc. 164 (2017) A1866–A1872.

III. **M. Härmas**, R. Palm, T. Thomberg, R. Härmas, M. Koppel, M. Paalo, I. Tallo, T. Romann, A. Jänes, E. Lust, Hydrothermal and peat-derived carbons as electrode materials for high-efficient electrical double-layer capacitors, J. Appl. Electrochem. 50 (2020) 15–32.

IV. **M. Härmas**, T. Thomberg, A. Jänes, Effect of Zinc Chloride Activation on D-Glucose Derived Carbons Based Capacitors Performance in Ionic Liquid, J. Electrochem. Soc. 167 (2020) 080533.

Author's contribution:

Paper I: Performed the synthesis and electrochemical characterization of the carbon materials. Participated in the preparation of the manuscript.

Paper II: Performed the synthesis and electrochemical characterization of the carbon materials. Participated in the preparation of the manuscript.

Paper III: Performed the synthesis and electrochemical characterization of the carbon materials. Participated in the preparation of the manuscript.

Paper IV: Performed the synthesis and electrochemical characterization of the carbon materials. Mainly responsible for the preparation of the manuscript.

2. ACRONYMS AND SYMBOLS

3. INTRODUCTION

Since the conventional power plants (wind, solar, hydro, nuclear, etc.) do not fit in the pocket, there is an ever-increasing problem of needing better and better energy storage devices. A part of the solution seems to come in the form of electrical double-layer capacitors (EDLC) that are considered the instruments of choice for many high-power applications. As such, EDLC is commercially considered to be inexpensive in terms of power capability (<1 EUR kW^{-1}) but costly in terms of energy storage capability (>4500 EUR $(kWh)^{-1}$) therefore EDLC are often used in high power devices. In general, the performance of EDLCs is expected to improve in terms of energy density and price while using readily available, cheap, and non-toxic materials. Additionally, mobile and stationary applications have somewhat different requirements for EDLCs [1]. The functionality of an EDLC originates from the reversible and fast (milli-seconds to seconds) adsorption of electrolyte ions in the electrode|electrolyte interface [2–4]. In general, EDLC can have capacitance values up to hundreds of farads per gram, orders of magnitude higher than well known dielectric capacitors. This difference is attributable to the nanoscopic (<1 nm) charge separation distance found at the electrode|electrolyte interface and huge specific surface area (SSA) that can go up to ~2600 $m^2 g^{-1}$ (single-layered graphene) [5–7]. Compared to the state of the art lithium-ion batteries, the EDLC deliver substantially lower energy densities but also endure several orders higher cycle life values. These properties make batteries and EDLC complementary and thus are often used in parallel in electric circuits [8].

Porous carbon materials are the most common electrode material used in EDLC due to the abundance of precursors, tunable porous structure and high achievable SSA values [9–11]. Although other aspects of EDLC (separator, electrolyte, design, etc.) also have a profound effect on the performance of the EDLC device, the electrodes are considered to have the highest impact on the overall cost and weight of EDLC [1].

Therefore this dissertation mainly focuses on the synthesis of novel carbon materials that can be used in a high power EDLC system as electrode materials. Additionally, the current study brings attention to the core parameters of the carbon material that contribute to the experimental power characteristics of a two-electrode device based on collected electrochemical and physical characterization data. As the activated carbons studied are highly disordered and with complex microstructure, an empirical approach was chosen to further optimize the electrode-electrolyte interactions and, thus, the overall performance of the EDLC device.

4. LITERATURE OVERVIEW

4.1 Supercapacitors

The term supercapacitor (SC) was coined in 1975, but the phenomenon of storing electrical energy into electrode|electrolyte interface has been described as far back as 1879 [12]. SC is a device that bridges the gap between the high energy density devices like batteries and fuel cells and high power density devices such as ceramic capacitors (used widely in circuits) (Fig. 1).

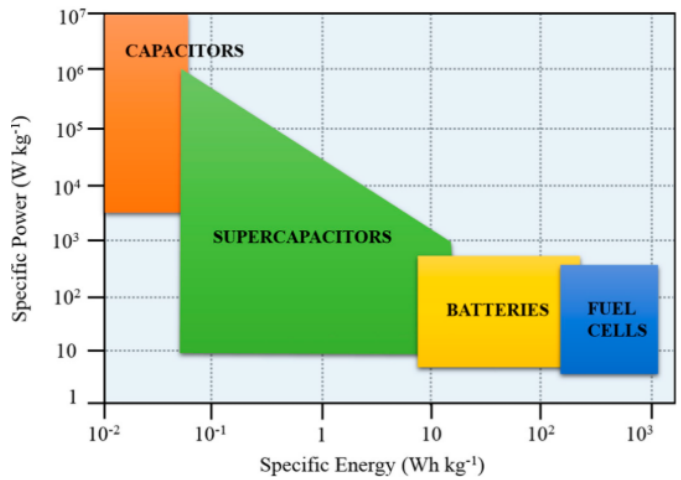

Figure 1. Sketch of Ragone plot for various energy storage and conversion devices [13,14].

For an ideal capacitor, the amount of charge, Q, stored on electrodes is linearly dependent on cell potential ΔV and system-specific content called capacitance C, or in mathematical terms [15]:

$$Q = C\Delta V \tag{1}$$

In the current peer-reviewed literature, the terms ultracapacitor and electro-chemical capacitor are used as a synonym for SC, but the first two are less common. SC can be roughly divided into two subcategories based on the energy storage mechanism: EDLC and pseudocapacitors. The main difference is that the latter technology utilizes materials with faradic reactions capabilities (RuO_2, MnO_2) that exhibit properties where electrode potential is proportional to redox species surface coverage and, therefore, proportional to the state of charge. Thus, giving rise to a linear dependence of the charge stored vs potential

mimicking adsorption process. The redox capabilities give them increased capacitance and energy density values compared to EDLC, but lower cycle life. The complementary electrode for pseudocapacitors is usually a double layer capacitive electrode, such as activated carbon. That means the term pseudo-capacitive should only be used in a system containing the faradaic electrode [15,16].

On the contrary, the term EDLC can be used both in two and three-electrode setup since both electrodes are capacitive (usually activated carbon). It is quite easy to complete a working SC since the components are rather straightforward (Fig. 2). The slightly more difficult task is to optimize the device to unlock the full potential. For that, there are different parameters to keep in mind.

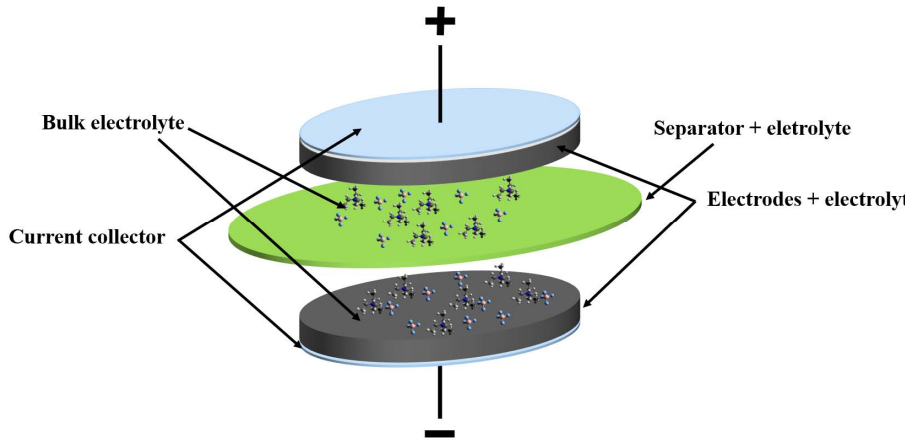

Figure 2. The layout of a two-electrode SC cell.

The SC is primarily used to supply high power to systems. Therefore power density is one of the most important parameters for comparing different SC. For the most simple case, the power P can be found using:

$$P = \Delta V I = \frac{(\Delta V)^2}{4R_{\mathrm{ES}}}, \tag{2}$$

where ΔV is cell potential, I is current and R_{ES} is effective series resistance that combines electrode surface layer, electrical contacts, and electrolyte resistances. The energy lost described by R_{ES} is usually released as heat.

Similarly, an important parameter for SC is the energy that determines how long the power burst lasts. Energy E can be calculated via:

$$E = \frac{C(\Delta V)^2}{2} \tag{3}$$

Equations 1–3 describe well the operating principles of an ideal EDLC. However, for a real device meant for a particular role in a device, there are many more parameters to take into account, such as operating temperature, decomposition potential, leakage current, cycle life, energy storage efficiency, etc. Since all of these parameters stem from the choice and combination of individual components, it is important to discuss these characteristics in detail [15].

4.1.1 Carbon as electrode material

Over the years, a lot of emphases have been put on developing new electrode materials to improve the charge storage performance of EDLC [15]. Electrode material fulfills one of the most influential roles in terms of the performance of a device. Therefore there are key properties that a potential electrode material must meet. To name a few: high SSA, well-developed micro- and mesoporosity, chemical and thermal stability, good electrical and heat conductivity, tailorable porosity, low-to-moderate costs, and ease of processability. Material that utilizes carbon in a different configuration (i.e. activated carbon, graphene, carbon onions, etc.) usually possesses these qualities and therefore are widely used in EDLC applications [1,17].

Estimates of carbon abundance vary substantially, but overall it is considered to have around 180 ppm concentration in Earth's crust that places this element barely in the top 20th most abundant element [18]. However, the same cannot be said about the importance of the element as entire organic chemistry and the reader of this paper is vastly based on carbons half-filled valence cell electrode configuration. The resulting sp, sp^2 and sp^3 electron configurations determine the geometry and nature of the carbon-carbon bonds in materials and the resulting physical and chemical properties [17,18]. For amorphous carbons, one of the most influential parameters is the number of π bonds that determines the electronic conductance [19,20]. Although sp^2 and sp^3 electron configurations can give rigid structures, it is quite common that a minimal amount of binder is added to the carbon material to optimize the physical durability of carbon electrodes [1].

4.1.2 Electrolytes

The electrolyte fulfils one of the most influential roles in SC, providing mass transport of ions that enables the formation of an electrical double layer and charge compensation on charging and discharging. The electrolyte is also considered to be the heel of Achilles in terms of maximum operating cell potential (ΔV) that SC device can operate. Exceeding ΔV leads to an electrochemical decomposition of the electrolytes (solvent + salt) that results in the ageing and failure of SCs. Since the electrochemical stable potential window is quadratically related to power and energy density (Eq. 2 and 3), a lot of emphases have been put to developing novel electrochemically stable electrolytes. In addition to the potential window, the electrolyte also influences or defines several other

key parameters such as internal resistance, operating temperature range, self-discharge rate, flash point and toxicity.

Besides stand-alone parameters, interactions of electrolyte with the electrode materials and separator also has a high impact on SC performance. Most importantly, choosing a complementary ion size to match porous parameters of the electrode material is crucial for maximizing specific capacitance value [10,21].

There are different types of electrolytes that each has advantages and disadvantages. Aqueous electrolytes have been thoroughly incorporated in SC research due to very simplistic laboratory needs and low overall cost. Aqueous electrolytes exceed at high ionic conductivity (generally at least order of magnitude higher than organic and ionic liquids), which is shadowed by marginally lower ΔV value (thermodynamic limited to 1.23 V). Besides that, aqueous electrolytes can also heavily limit the applications of the device in colder climates to the risk of freezing and rapturing the device.

In terms of commercial SC, the lion's share uses organic electrolytes [1,22]. Organic electrolytes are widely used since they have relatively wide ΔV (2.5–2.8 V, sometimes up to 3.0 V), while still maintaining reasonable values for conductivity and viscosity [21,22]. Compared to aqueous electrolytes, the organic electrolytes are significantly more expensive due to bulk prices of solvent and salt and due to additional cost relating to solvents sensitivity towards water vapour and oxygen. This is a significant factor since electrolyte can make up to 27% of the overall cost of the device. Therefore it is estimated that the electrolyte price range should not exceed 12 EUR kg^{-1} [1].

Ionic liquids (IL) are attractive third options as an electrolyte. An IL consist of a large asymmetric organic cation and an inorganic or an organic anion that is due to the sterical reason in the liquid phase at room temperature. IL stand out with their high thermal, chemical and electrochemical stability, negligible volatility (room temperature), and high flash point. Alas, most ionic liquids also exhibit high viscosity, low ionic conductivity and high cost, being the main reasons why IL as an electrolyte, has not made a break to commercial SC applications [21].

4.1.3 Separator materials

SC separator functions as an electronic insulator between two electrodes dampening the electric field down to a point where no electrical shorting can happen. Additionally, SC separator must allow relatively good ionic permeability and be chemically stable in operating conditions. Separators also have a pivotal role in self-discharge processes by controlling the active migration of electrolyte ions [23]. To facilitate ionic transport, the separator is typically made up of porous polymeric membranes like cellulose nitrate, polyvinylidenefluoride (PVDF), polytetrafluoroethylene (PTFE) membrane [15]. However, some flexible SC devices use solid electrolytes that effectively cover the role of a separator [24].

4.2 Production of carbonaceous material via hydrothermal carbonization

Using water at high temperatures is a simple green and a very attractive way of converting low-cost biomass into highly functional materials. Based on the main product obtained these processes can be categorized into hydrothermal carbonization (usually 100–200 °C), hydrothermal liquefaction (typically 200–350 °C) and hydrothermal gasification (usually 350–750 °C) [25]. In recent years the hydrothermal carbonization (HTC) has been successfully applied for preparation of low-cost porous carbon used in different fields such as energy storage, adsorption and soil improvement [26–28]. HTC process takes place below the critical point of water (T_c = 373 °C, p_c = 22.1 MPa) that nevertheless alters some of the solvents physical and chemical properties (ion product, density, static dielectric constant) heavily compared to ambient water [25,29]. Many reactions take place dependent on the HTC process precursor and the detailed nature of the reaction pathways is not always fully understood yet. Therefore simple carbohydrates (e.g. D-glucose) are often used as model precursors in order to study their transformation mechanism into HTC materials. The decomposition of sugars starts with hydrolysis due to having lower activation energy than most of the other reactions. Hydroxymethyl furfural (HMF) and furfural are well-known dehydration products of sugars [28,30]. The reaction intermediates and the HMF product can further react or degrade by processes such as isomerization, condensation, rehydration, reversion, fragmentation and/or additional dehydration reactions [31]. The main outcome of the HTC process is the solid carbonaceous product named hydrochar (sometimes also called hydrothermal carbons or humins). In the case of pentoses and hexoses, these hydrochars consist of micrometre-sized spheroids that exhibit a core-shell structure of chemical oxygen functional groups [32,33]. In addition to the hydrochar, small organic acids (e.g. levulinic acid) and gaseous by-product are also formed. The formation of organic acids is useful since it selfcatalyses the process, advancing the necessary dehydration reactions [30].

4.2.1 Chemical activation of carbonaceous material

Chemical activation is considered an effective method for increasing porosity of carbonaceous materials, thus directly (Eq. 3) increasing energy storage capabilities of EDLC [34,35]. There are two industrial processes used to maximize the adsorption potential of a parent organic material: physical (also known as thermal activation, utilizing reagents such as CO_2 and H_2O) and chemical activation (using reagents such as $ZnCl_2$, H_3PO_4 and KOH) [35–38]. The often-used terminology (chemical/physical activation) is somewhat misleading since both types of activation processes make use of chemical reactions; therefore, these processes are referred henceforth as oxide activation (OA) and acid-base-salt (ABS, referring to Lewis acid-base definition) activation respectively.

For the individual application of carbon material-specific control of pore-size distributions is required, that is achieved by selecting appropriate activating agents and treatment condition combinations. Since, in OA, such variables as temperature, pressure, heating rate, etc. do not influence the micropore size distribution significantly using the alternative ABS activation is often more appealing for since it allows more control over the product characteristics [36,39]. On the other hand, ABS activation is also considered to be more corrosive and is often paired with an additional washing step compared to OA activation [40].

The ABS activation usually involves mixing the precursors (carbon source) and activating agent and then heat-treating the mixture at inert atmosphere. As a result, abundant micropores or mesopores are formed in the carbon framework after washing out the residual activating agent and by-products [10,37].

ABS activation of hydrothermal carbons has been the focus of a great number of studies [27,41–46], but Sevilla et al. [47] are considered to be the first to report on the ABS activation of HTC materials as a way to generate highly porous materials [48].

4.2.1.1 Activation with $ZnCl_2$

In the case of $ZnCl_2$ activation, the reactant is essentially a template for the creation of porosity as increases in microporosity is roughly equal to the volume of $ZnCl_2$ used. Space is vacated after this reactant vaporizes (T_B = 732 °C) or after washing is conducted. Most of the porosity develops within the temperature range of 400−500 °C, whereas an increase in temperature leads to increasing microporosity [35,49].

4.2.1.2 Activation with KOH

In contrast to zinc chloride, KOH reacts directly with the carbon. Based on Fourier-transform infrared spectroscopy data, thermal desorption spectroscopy data and Gibbs free energy calculations results, the following reaction is proposed:

$$6KOH + C = 2K + 3H_2 + 2K_2CO_3 \quad (4)$$

Many experimental variables influence activation processes such as reactivity of the starting carbon, the ratio activating agent/carbon, the method of mixing of the activating agent and carbon, the temperature and flow of gas during the carbonization, etc. In general, KOH reaction with carbon begins at around 400 °C, whereas in case of NaOH it started only at 570 °C. At temperatures higher than 800 °C, the decomposition of the carbonates starts, that results in the evolution of CO and CO_2 [38,50,51].

4.3 Methods for electrochemical characterization of EDLC

4.3.1 Cyclic voltammetry

Cyclic voltammetry (CV) or linear sweep voltammetry is a versatile method that is based on applying a linearly varying potential across the two electrodes of a two-electrode device, or between the working and reference electrode in a three-electrode system. The initial potential V_i is swept linearly in time v (V s^{-1}) so that potential at any time $V(t)$ can be found:

$$V(t) = V_i - vt \tag{5}$$

The resulting current is registered. In the case of the ideal capacitor, the current response $I(t)$ is equal to:

$$I(t) = C\frac{dV}{dt} = Cv \tag{6}$$

Therefore for symmetrical two-electrode cell, the specific capacitance of a single electrode C_{CV} can be found:

$$C_{CV} = \frac{2I}{vm}, \tag{7}$$

where m is the mass of a single electrode [10,52].

CV is a very popular technique for initial electrochemical studies of new systems and has proven very useful in obtaining information about fairly complicated electrode reactions. In EDLC applications is mainly used for determining maximum operating cell potential, calculating corresponding capacitance values and providing rough estimates of faradaic processes [15,17,52,53]. In the case of redox-active species at semi-infinite linear diffusion conditions, the current at any point can be estimated by:

$$i = nFAC_O\sqrt{(\pi D_0 \sigma)}x(\sigma t), \tag{8}$$

where n is the stoichiometric number of electrons involved in an electrode reaction, F the Faraday constant (charge on one mole of electrons), A cross-section area of an electrode, C_O the concentration of oxidized form, D_O the diffusion coefficient of oxidized form and $\sigma t = nFvt/RT$ and $x(\sigma t)$ a pure number current function [53]. This essentially means that in case of redox reactions the current response is proportional to the square root of scan rate while in case of the non-faradaic process such as adsorption, the response is simply linear (Eq. 6). Unfortunately, both the double-layer and faradic processes occur at almost the same timescale making them practically indistinguishable if applying only the CV method [15].

If the capacitance is constant with potential, the ideal current response, according to Eq. 6 is rectangular (Fig. 3). However, real-life SC system has internal resistances that have linearly increasing impact on CV curves as the v value increases. Besides resistance, faradaic reactions (battery type electrodes and pseudocapacitive electrodes) also can change the current response of the SC system (Fig. 3) significantly. However, there are also some pseudocapacitive materials, which have almost similar cyclic voltammograms as that of an ideal double-layer system [15].

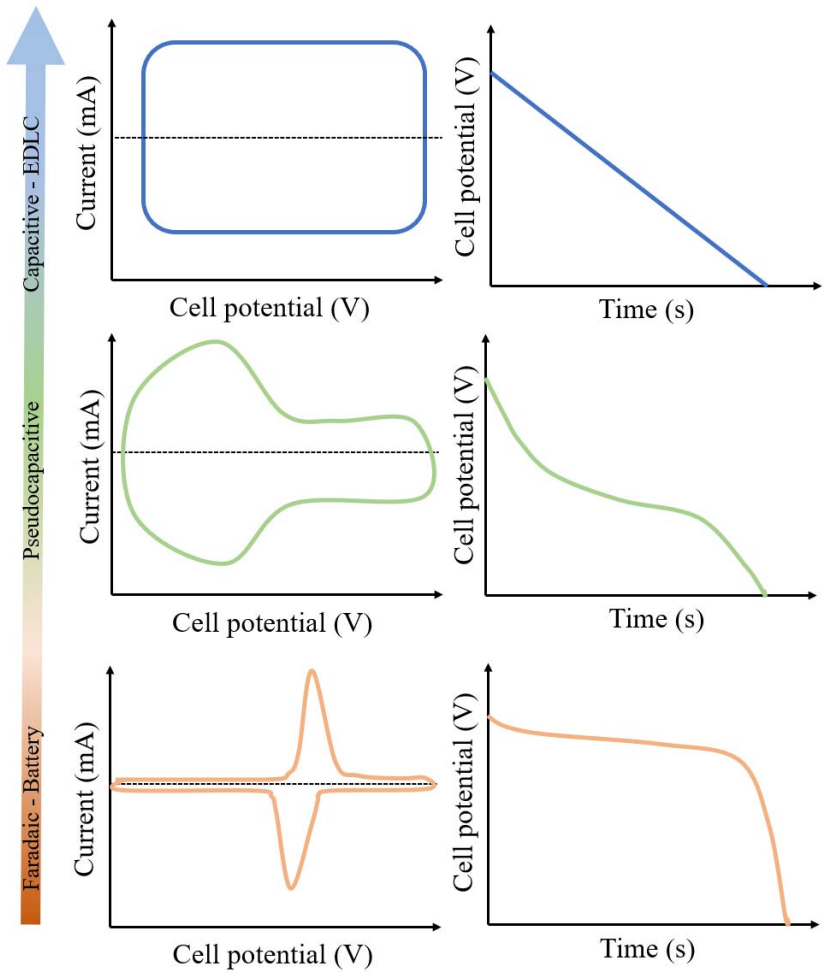

Figure 3. Schematic cyclic voltammograms (top) and corresponding galvanostatic discharge curves (bottom) for various kinds of energy storage materials [15,52].

4.3.2 Controlled current method

The constant current charge/discharge (CCCD) method is widely used both for SC and battery research since the implementation is easy and cheap. CCCD method is based on applying constant current input during the charging and discharging of supercapacitor device or a single electrode (in three-electrode configuration). Here, the registered potential varies as a function of time with an applied constant current. Similar to the CV technique, the shape of the output curve provides important information regarding the charge storage process along with iR drop, the percentage contribution to double-layer and faradic charge storage, and effective series resistance (R_{ES}) of the supercapacitor device.

In a real-life device, the Fig. 3 discharge curve is preceded by a sharp potential drop caused by the ohmic current flow in combination with charge recombination and self-discharge effects. Therefore the discharge capacitance (C_{DC}) for EDLC should be calculated using the linear cell potential difference region of discharge curve via:

$$C_{\mathrm{DC}} = I\frac{\Delta t}{\Delta V} \tag{9}$$

For specific discharge capacitance of symmetrical device for a single electrode, this can be written as:

$$C_{\mathrm{DC}} = \frac{2I\Delta t}{\Delta V m}, \tag{10}$$

where m is the mass of an electrode [17,54].

CCCD method is frequently used to calculate the efficiency of a device. The efficiency of SCs is very often presented as coulombic efficiency that is based on the simple ration of charge and discharges time values. Coulombic efficiency can be misleading as it assumes a linear response that is often not the case, especially for SC system utilizing faradaic reactions. Energy efficiency (η_{ef}) is a better parameter since it takes into account the non-linearity of some CCCD curves by integrating, i.e. finding the ratio of areas under the constant discharge (CD) vs constant charge (CC) curve. η_{ef} can be found:

$$\eta_{ef} = \frac{E_{\mathrm{DC}}}{E_{\mathrm{CC}}} = \frac{\int_{t(V_{\min})}^{t(V_{max})} V(t)dt}{\int_{t(V_{min})}^{t(V_{max})} V(t)dt}, \tag{11}$$

where E_{DC} and E_{CC} are discharging and charging energies, respectively [54].

4.3.3 Electrochemical impedance spectroscopy

For CV and CCCD methods, the system under study never reached equilibrium state during the experiment due to the large perturbations used. Electrochemical impedance spectroscopy (EIS) however uses small magnitude alternating perturbation (usually potential, but equal result can be obtained via using current, Eq. 11) where the response may be indefinitely steady and can, therefore, be averaged over a long term. With stable systems, the EIS can be implemented over a wide time (or frequency) range (10^4 to 10^{-6} s or 10^{-4} to 10^6 Hz). Often the perturbation is applied as a sinusoidal wavefunction:

$$V(t) = V_0 \sin(\omega t)\,, \tag{12}$$

where $V(t)$ is time dependent potential (Fig. 4), V_0 perturbation amplitude (usually couple of millivolts), ω angular frequency $\omega = 2\pi f$, f is the frequency (Hz) [17,53].

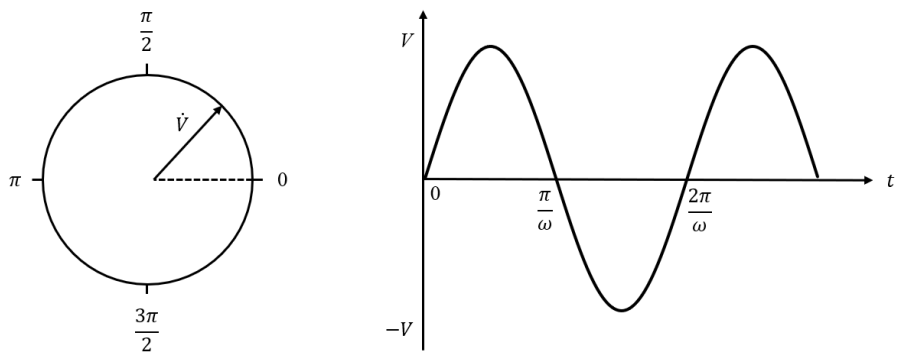

Figure 4. Phasor diagram for an alternating potential $V(t)=V_0\sin(\omega t)$.

A common way to visualize the alternating potential is as a rotating vector (or phasor, $\dot{V}$). The length of the vector represents the peak amplitude and the direction the timeframe of the phase value. The corresponding current is then expressed similarly as a sinusoidal wave:

$$I(t) = I_0 \sin(\omega t + \varphi)\,, \tag{13}$$

where I_0 is the current amplitude (Fig. 5).

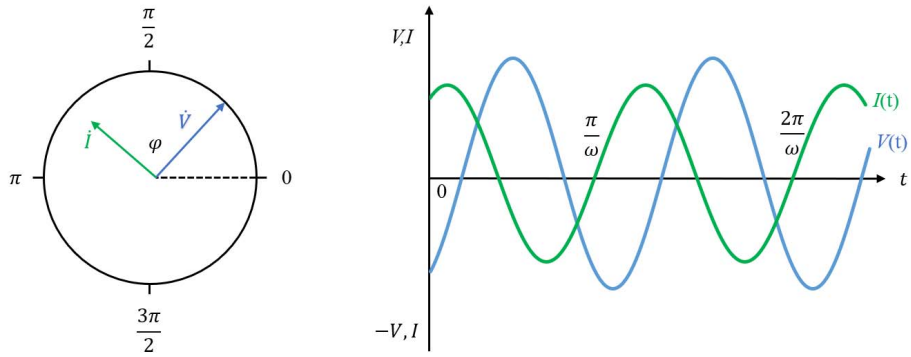

Figure 5. Phasor diagram for an alternating potential $V(t)$ and current $I(t)$.

As shown in Fig. 5, the current $\dot{I}$ and potential $\dot{V}$ are often out of phase at all times, meaning that the two rotating vectors are separated by phase angle φ. On the graph, the potential is lagging the current and for the ideal capacitor, the φ value is 90° or π/2 radians [53].

Ohm's law always holds. Therefore a linear relation exists between the current and the potential at each moment:

$$Z(t) = \frac{U(t)}{I(t)} = \frac{\dot{U}}{\dot{I}} \tag{14}$$

Since both current and time are vectorial quantities, the impedance $Z(t)$ is also a vector quantity. Z is often measured over a wide range of (angular) frequencies to probe different electrochemical processes at different timescales. $Z(\omega)$ is also called complex impedance since it can be expressed as a complex number of the vector sum of real (Z' or Z_{Re} and imaginary (Z'' or Z_{Im}) parts:

$$Z(\omega) = Z'(\omega) + Z''(\omega)\,, \tag{15}$$

where $i = \sqrt{-1}$. Since the Pythagorean theorem still holds, the modulus can be written as:

$$|Z(\omega)| = \sqrt{Z'(\omega)^2 + Z''(\omega)^2} \tag{16}$$

and the phase angle as:

$$\varphi(\omega) = \arctan\left[\frac{Z''(\omega)}{Z'(\omega)}\right]. \tag{17}$$

For ideal RLC (resistor, an inductor, and a capacitor) circuit, these parameters are the following:

Element	$\|\boldsymbol{Z}\|$	$\boldsymbol{Z'}$	$\boldsymbol{Z''}$	$\boldsymbol{\varphi}$
Resistor	R	R	0	0
Inductor	ωL	0	ωL	90°
Capacitor	$\frac{1}{\omega C}$	0	$\frac{1}{i\omega C}$	–90°

Real-life EDLC systems are a bit more complicated. For the simplest of cases, the of RC circuits the resistor and capacitor in series and parallel are often used to model the low-frequency part where capacitive processes start to dominate complex impedance. Series capacitance C_S, series resistance R_S, parallel capacitance C_P and parallel resistance R_P can be calculated via:

$$R_S = Z'(\omega) \tag{18}$$

$$C_S = -\frac{1}{\omega Z''(\omega)} \tag{19}$$

$$C_P = -\frac{1}{\left(1 + \left|\frac{Z'(\omega)}{Z''(\omega)}\right|^2\right)\omega Z''(\omega)} \tag{20}$$

$$R_P = \frac{\left(1 + \left|\frac{Z'(\omega)}{Z''(\omega)}\right|^2\right)\omega Z'(\omega)}{\left|\frac{Z'(\omega)}{Z''(\omega)}\right|^2}. \tag{21}$$

These simplistic ac circuit models are relatively easy to apply, but unfortunately, a single resistor cannot describe the characteristics of the real-life application under variable load. For more complex systems a very popular and informative way of representing the impedance behaviour of is by plotting Z'' versus Z'components for a range of frequencies in a Nyquist plot.

Nyquist plot for a typical EDLC impedance spectrum composes of three parts: the low frequency nearly vertical region, the –45° slope region at intermediate frequencies and the high-frequency depressed semi-circle region [14,17,52,55]. For better understanding, the electrochemical systems numerous theoretical model has been developed. Models developed can be grouped into three categories based on the description of the system. At the most fundamental level are the atomistic or microscopic models, describing the individual charge-carrying particles. At the least detailed level are the equivalent circuit

models that try to construct a simple circuit with well defined electrical properties that mimic the response signal. At the intermediate level are the continuum models regarding the bulk matter as continuous media. From a practical point of view, all three types of models are useful and provide ways to further explain and predict the behaviour of electrochemical systems [55]. A common model for the high-frequency semicircle is to use parallel RC circuit (Fig. 6) where the two cutting points with the Z' axes used to define the R_{ES} and potential dependent faradaic resistance R_F values for redox-active species [52,55].

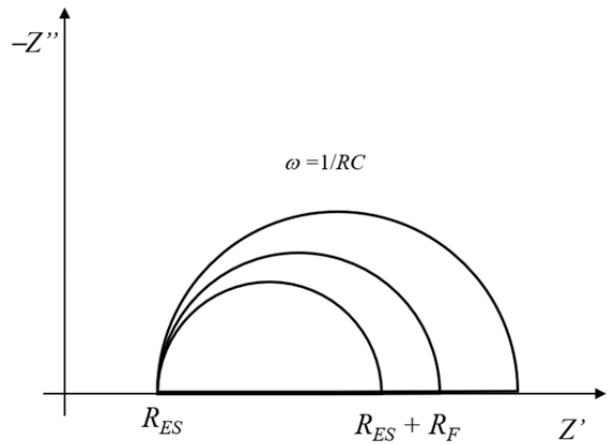

Figure 6. Nyquist plot for a parallel RC circuit.

The –45° slope region at intermediate frequencies is often associated with diffusion control in the kinetics of the electrode process. This region is usually controlled by Fick type diffusion and modelled with Warburg semi-infinite diffusion element. The frequency and the pore radius defines the penetration depth of λ_w the initial perturbation wave via:

$$\lambda_w = 12\kappa r C_d \omega \,, \tag{22}$$

where r is the pore radius (cm), κ is the electrolyte conductivity (Ω^{-1} cm^{-1}), C_d is the electric double-layer capacitance at the interface (F cm^{-2}), and ω is the angular frequency (rad s^{-1}). This means that at lower frequencies, more pores are accessible to excitation until a specific knee frequency where all surface of the electrode is active and capacitance is no longer frequency dependent [56].

Based on the pseudo-3D numerical modelling of Keiser et al. [57], the low-frequency region impedance spectra is also highly dependent on the pore geometry (Fig. 7). Unfortunately, the shape of the pore model is rather hard to implement on real-life samples data since materials like amorphous carbon are heavily nonhomogeneous and mostly lack ordered structures.

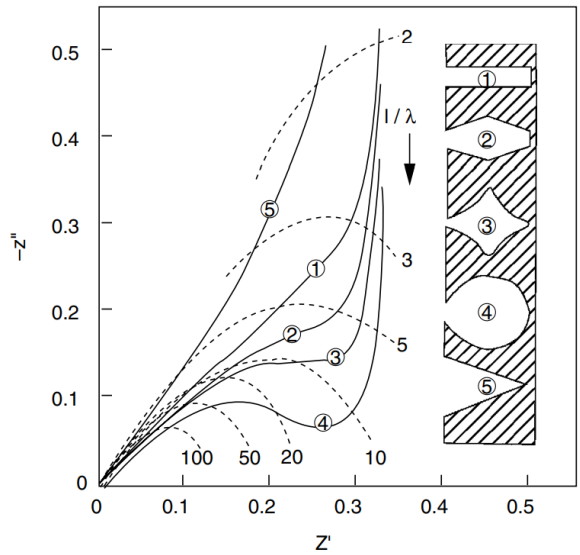

Figure 7. Impedance behaviour for a series of pore shapes, as shown, in a porous electrode. *l* is pore length and λ is a form factor [57].

4.4 Gas sorption – probing the porous structure of materials

Gas sorption analysis is one of the most popular methods that allow the characterization of materials surface area and pore size distribution (PSD). The method is based on measuring the volume or mass of adsorbate (usually N_2, CO_2 or Ar) at various pressures under either static and quasi-equilibrium conditions. The resulting isotherm is thereafter analyzed by applying an appropriate theory used to treat the adsorption and/or desorption data.

Many activated carbons exhibit type I sorption isotherms that correspond to microporous materials [58]. Based on IUPAC classification, pore widths greater than 50 nm are called macropores, mesopores range from 2 to 50 nm and micropores for the pores in the range of less than 2 nm [59,60]. Microporous type I isotherm can be described by the Langmuir equation:

$$\frac{p}{W} = \frac{1}{KW_n} - \frac{p}{W_n}, \tag{23}$$

where W and W_n are the weight adsorbed and the weight adsorbed in a completed monolayer, respectively. p is the adsorbate pressure and K is Langmuir constant that depends on the interaction energy between adsorbate and adsorbent.

Brunauer, Emmett, and Teller (BET) further developed the Langmuir model to incorporate multilayer adsorption and the linearised form of BET equation is often used to calculate surface area values for microporous materials. Despite the often reported good fit to the experimental data, the obtained surface area results should be taken with a grain of salt since it does not reflect a true surface area.

Microscopic methods (such as Non-local Density Functional Theory, NLDFT and Grand Canonical Monte Carlo simulation) are considered to have a much more accurate pore size analysis and allows in principle to perform a pore size analysis over the complete micro/mesopore size range. Although applying NLDFT requires using appropriate adsorptive/adsorbent system kernel and often the model does not fit the experimental results perfectly. Therefore, the microscopic methods are still considered the most accurate methods for analyzing porosity data [61].

One of the most informative parameter that NLDFT models enable to explore is PSD. The evaluation is based on solving the adsorption integral equation:

$$a_{exp}(p) = \int_{w_{min}}^{w_{max}} a_{loc}(p,w) f(w) dw \,, \tag{24}$$

where $a_{loc}(p,w)$ is the local adsorption isotherm (kernel function), $a_{exp}(p)$ is the experimental isotherm and $f(w)$ is the PSD function.

In the recent decade, the two large instrument companies Micromeritics Instrument Corporations and Quantachrome Instruments have introduced 2D-NLDFT and QSDFT models, correspondingly, both of which try to take into account the geometric heterogeneity of the adsorbent surface. The QSDFT model addresses heterogeneity the surface via roughness factor (quenched component) and 2D-NLDFT models the surface of pore wall via randomly wrinkled graphene sheet. Despite the differences, both the QSDFT and the 2D-NLDFT methods give similar valid PSD values [62].

5. EXPERIMENTAL

5.1 Synthesis of electrode materials

Studied electrode materials were prepared via a two-step process. The initial carbonaceous material was synthesized using a high-pressure autoclave (Büchi limbo) via HTC process. Synthesis conditions (200° C for 24 h) were chosen to ensure maximum solid product yield while maintaining the structural integrity of the vessel. After that, the carbonaceous material was collected and washed with Milli-Q+ water for several times and dried overnight in a vacuum oven (Vaciotem-TV, J.P. Selecta) at 120° C and 50 mbar to ensure removal of water. The yield of the product is often reported as the ratio of masses rather than the traditional reaction yield since often no clear and fixed reaction equation cannot be attributed to the process [63–66]. In the case of mono and disaccharides precursors, 35–40% yields were calculated for studied materials.

Since the HTC materials do not have suitable porosity for supercapacitor applications, an additional activation procedure was carried out. As an interesting and less refined alternative to HTC materials, a patch of dried and washed peat was also used as a precursor material for activation since it bares similar drawback as HTC materials. Therefore all of the intermediate materials were mixed with activating reagents (KOH, $ZnCl_2$) in an aqueous medium to facilitate the transport of activating reagents to the already existing porous matrix. Thereafter the water was removed in mild conditions (vacuum oven) since water can also alter the porous structure of carbon materials. The activation was carried out in alumina crucible that was then put into the tube furnace (Carbolite CTF 12/65/550) after that the impregnated and dried mixture was pyrolyzed at 700° C for 2 h at Ar atmosphere. 700° C is not necessarily the optimal temperature for KOH and $ZnCl_2$ to achieve maximum SSA (see section 4.2.1). The temperature was chosen since the thermal treatment also alters the graphitic structure of the materials and we wanted to compare different activating reagents without secondary effects. After activation, all of the samples were washed with Milli-Q+ water several times, then treated with hydrochloric acid to remove the excess of activating agents and the residuals and washed again with Milli-Q+ water.

The resulting activation yields were somewhat dependent on the amount of impregnation mixture used (since numerous the treatment steps remove a quantity of material) and the ratio and activating reagent used. Yields achieved were as large as 66%, when more than 6 g of impregnation mixture was used. The final treatment of all carbon materials was reducing the surface functional groups with H_2 (purity 99.9999%) at 800° C for 2 h.

The resulting carbon materials were named via a combination of the name of carbonaceous precursor material and the name of activating reagents (KOH and $ZnCl_2$) as follows:

Glucose derived carbon	**GDC**	
White sugar derived carbon	**WSDC**	+ **Activating Reagent (**KOH and $ZnCl_2$)
Peat derived carbon	**PDC**	

5.1.1 Electrode preparation

As obtained activated carbons were powders, it was necessary to add some binder to obtain reproducible results and to improve electrical contact between the porous carbon particles. Most of the materials were prepared by adding 5% of polytetrafluoroethylene (PTFE, Sigma Aldrich) or up to 7% PTFE to obtain tenacious mass that could be roll-pressed (HS-160N, Hohsen Corporation, Japan) into ~110 μm thick sheets. After drying under vacuum, the pure Al layer (thickness of 2 μm obtained with QCMB, 1.5 μm with AFM) was deposited onto one side of the carbon material using the plasma-activated physical deposition method.

5.2 Electrochemical characterization

Electrochemical measurements were carried out in a two-electrode aluminium test cells (HS Test Cell, Hohsen Corporation). EDLCs were assembled in a glove box (Labmaster sp, MBraun, O_2 and H_2O concentrations lower than 0.1 ppm) by using two 2 cm^2 activated carbon electrodes and a commercial 25 mm thick separator (TF4425, Nippon Kodoshi). The test cell was filled with either 1 M triethylmethylammonium tetrafluoroborate (Et_3MeNBF_4) solution in acetonitrile (AN) or with 1-ethyl-3-methylimidazolium tetrafluoroborate ($EMImBF_4$) as electrolytes since both electrolytes are widely used in research [4,17,24,52].

The electrochemical characteristics of EDLCs were established by the electrochemical impedance spectroscopy (EIS), cyclic voltammetry (CV), constant current charge/discharge (CCCD) and the constant power (CP) discharge methods. Impedance spectra (over ac frequency range from 1 mHz to 300 kHz with perturbation of 5 mV), CV and CC curves were recorded using a frequency response analyzer 1252A and potentiostat SI1287 (Solartron, UK). The CP tests were carried out on a BT2000 testing system (Arbin Instruments, USA).

5.3 Physical characterization

5.3.1 Raman spectroscopy

Raman spectra were recorded using a Renishaw inVia micro-Raman spectrometer with Ar laser excitation beam (λ= 514 nm). Obtained spectra were baseline corrected using 4th order polynomial baseline and thereafter normalized relative to the G-band intensities. Data analysis was done using OriginPro software.

The first-order region of Raman spectra shows two distinct bands characteristic of amorphous carbon materials: one at Raman shift ~1330 cm^{-1} (D-band) and second at ~1590 cm^{-1} (G-band) [45,67–69]. The G-band is assigned to the

doubly degenerate Raman active E_{2g} in-plane vibration mode, which is attributed to the in-plane stretching motion of sp^2 carbon atom pairs. The presence of G-band indicates that the sample contains sp^2 carbon bonds. In contrary, the D-peak originates from defect-induced Raman features such as A_{1g} symmetry. This peak reflects the presence of disordered areas in carbon particles. The integrated D-band and G-band intensity ratio I_D/I_G is widely used to characterize the quantity of defects in graphic materials [45,70–73]. However, fitting the D- and G-peak area with only two peaks left a substantial fit residual between the D- and G-peak area and before D-peak. A better fit was obtained by using four Lorentzian functions [74,75].

5.3.2 X-ray diffraction

X-ray diffraction (XRD) patters of the activated carbon materials were acquired using Bruker D8 Advanced Diffractometer with Cu Kα1 radiation (1.540596 Å), Vario1 focusing primary monochromator, two 2.5° Soller slits and a LynxEye line detector. XRD patterns of the synthesized carbon material, exhibit very weak diffraction peaks corresponding to the graphite (hexagonal symmetry, space group $P6_3/mmc$) 002 peak at $2\theta \sim 25°$ and 100/101 peak at $2\theta \sim 43°$.

5.3.3 Scanning electron microscopy (SEM)

Characterization and imaging of the surface of activated carbons were conducted using a variable pressure Zeiss EVO MA15 scanning electron microscope, equipped with an Oxford X-MAX energy-dispersive detector system (EDS). Spectra were collected in variable pressure mode using 20 keV accelerating potential and focused electron beam and images were measured in secondary electrons mode.

5.3.4 Gas sorption

The nitrogen and carbon dioxide adsorption-desorption were carried out using an ASAP 2020 (Micromeritics, USA) and 3Flex (Micromeritics, USA) systems. The DFT specific surface area (S_{DFT}), pore volume (V_{DFT}) and pore size distribution data were calculated using fitting of N_2 isotherm data with "Carbon-N2-77, 2D-NLDFT Heterogeneous Surface" (SAIEUS v2.02, Micromeritics) model. As a comparison, Brunauer-Emmett-Teller specific surface area (S_{BET}) was calculated via multiple points method in the relative pressure (p/p_0) range from 0.05 to 0.1. The total pore volume (V_{tot}) was calculated from the amount of adsorbed nitrogen at relative pressure $p/p_0 = 0.995$.

6. RESULTS AND DISCUSSION

6.1 Physical characterization

6.1.1 XRD and Raman spectroscopy

As discussed earlier, the structure of activated carbon electrodes heavily influences the electrochemical behaviour of the SC device. Porous carbon obtained via the HTC process and ABS activation all exhibit rather amorphous structure, making it difficult to analyze in-depth, although some generalized data can be gathered. As can be seen in Fig. 8, characteristic XRD spectra for the materials under study show very little long-range repeating structures as a result of the random nature of particle growth in the HTC process. The diffraction reflexes seen in Fig. 8b can be attributed to graphite-like structures (hexagonal symmetry, space group $P6_3/mmc$) for 002 peaks at $2\theta \sim 24°$ and 100/101 peak at $2\theta \sim 43°$. At lower 2θ angle values, the signal also grows as larger structures dimensions are probed such as smaller macromolecules and micro- and mesopores [76]. All in all, there were very little differences between XRD patterns for synthesized activated carbons.

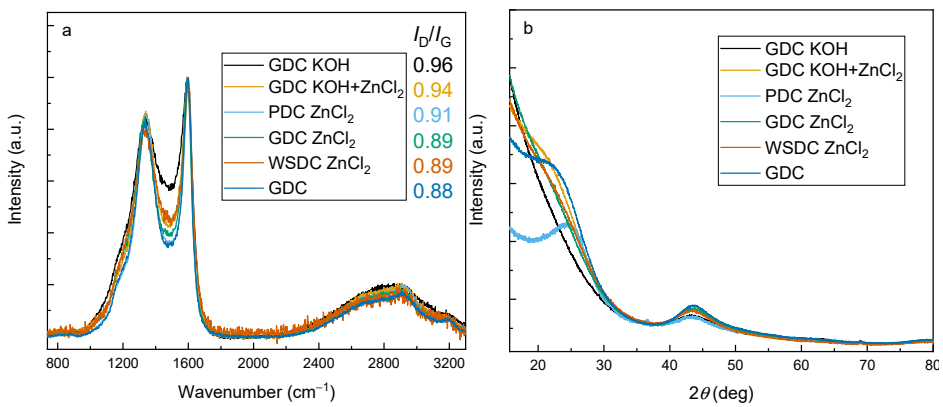

Figure 8. Raman spectra (a) and characteristic XRD patterns (b) for various activated carbons.

In conjunction with XRD, the Raman spectroscopy was used to further characterize the materials. Compared to XRD data, the signal for Raman originates from the structural vibrations, in addition, the probing wavelength and the interaction volumes are comparatively different in the case of Raman spectroscopy. Therefore, the information gathered from the two methods is fundamentally different, although the results gained are in both cases relate to the graphitic structure.

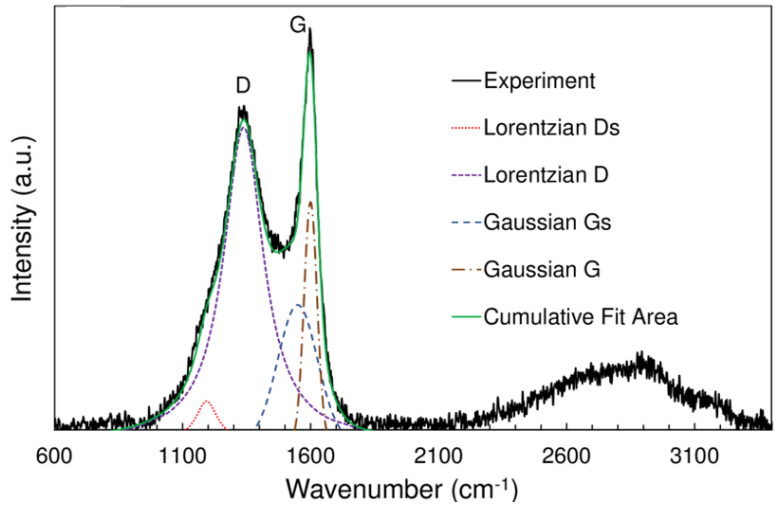

Figure 9. Raman spectra fitting for WSDC $ZnCl_2$ (similarly applied to all studied materials).

Raman spectra offer detailed information about the structure that can be used both quantitatively and qualitatively. Often empirical formulas are used for the interpretation of the Raman spectra of disordered carbons. However, the results of this quantitative analysis with empirical formulas have been shown to have errors as high as 100% [74,77–79].

All in all, the materials activated with KOH exhibited broad and overlapping D and G bands. Fitting the I_D/I_G (visualized in Fig. 9) revealed (Fig. 8) that the activation with KOH led to relatively more amorphous carbon structure compared to materials activated with $ZnCl_2$.

6.1.2 SEM results

Lateral contrast images highlight the different activation mechanism for KOH and $ZnCl_2$ (Fig. 10) vividly. For $ZnCl_2$ activated materials, the characteristic spherical particles of hydrochar precursor remain unchanged. In contrast, increasing KOH amount in impregnation mixture results in carbon materials that surface continuously changing into a more spongy structure, baring the marks of gasification reactions. It is visible that surface morphology strongly depends on the raw material. In case of not analytically pure sugar (WSDC $ZnCl_2$, Fig. 11) the resulting carbon spheres were larger in average and median diameter and had a mixture of smaller and bigger spherical particles present. For PDC, the raw material was even less homogeneous. The initial disordered structure remained similar after activation with $ZnCl_2$ and no spherical particles were detected at higher magnification values. (Fig. 11).

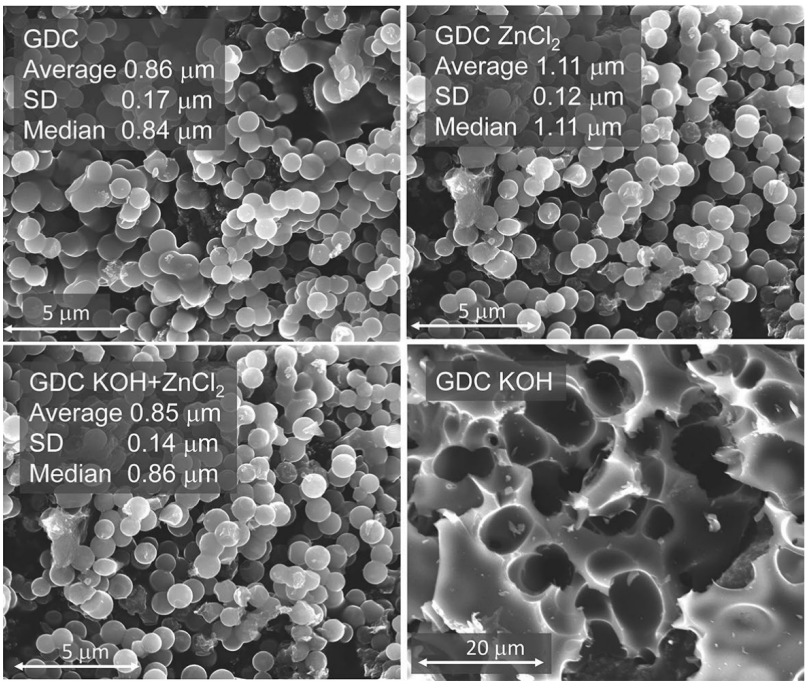

Figure 10. SEM images for GDC materials synthesized using KOH and $ZnCl_2$ with spherical particle size parameters (noted in the figure).

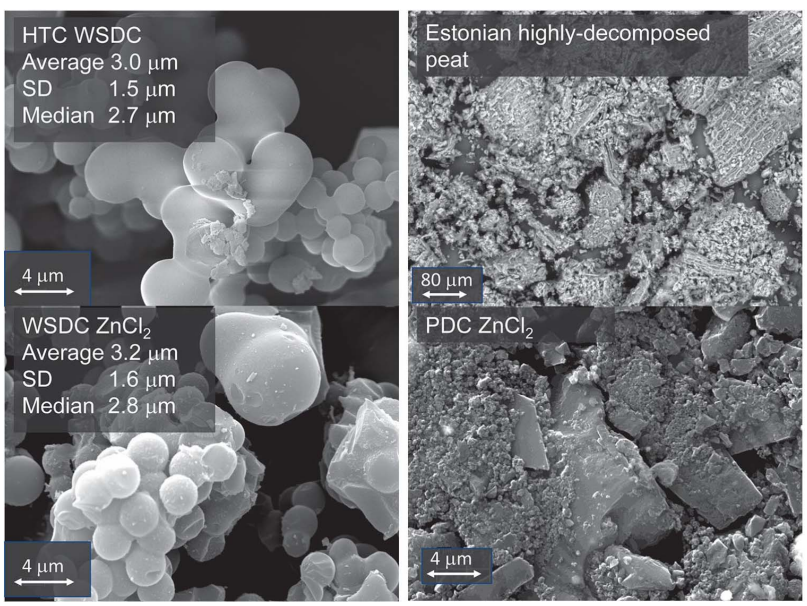

Figure 11. SEM images for hydrothermal carbons and carbon materials from granulated white sugar and peat with spherical particle size parameters (noted in the figure).

6.1.3 Gas sorption results

Activated carbon powders porosity was characterized via N_2 (Fig. 12a,b) and CO_2 (some materials) sorption measurements analysis and the main results are compiled in Table 1.

The activating reagents have enhanced the overall porosity of precursors and using higher quantities also improved the outcome. Unfortunately, the mixed activation resulted in less than hoped for results. That said, $ZnCl_2$ and KOH, if used separately, seemed to have yielded in similarly high surface area and total pore volume values. If only the values calculated by NLDFT are considered, the KOH activation enables to obtain superior results in SSA versus $ZnCl_2$ activation.

Pore size distribution (PSD) plots (Fig. 12c,d) reveal that the growth in surface area and total pore volume is caused by widening of pores in the smaller mesopores region (<3 nm). For PDC, the PSD highlights the scale of $ZnCl_2$ activation effect on organic precursor material as existing macrostructures remain mainly intact. Adding more $ZnCl_2$ seems to gradually widen the pores (Fig. 12b) enabling in concept the fine-tuning the materials to match the need of the specific EDLC application.

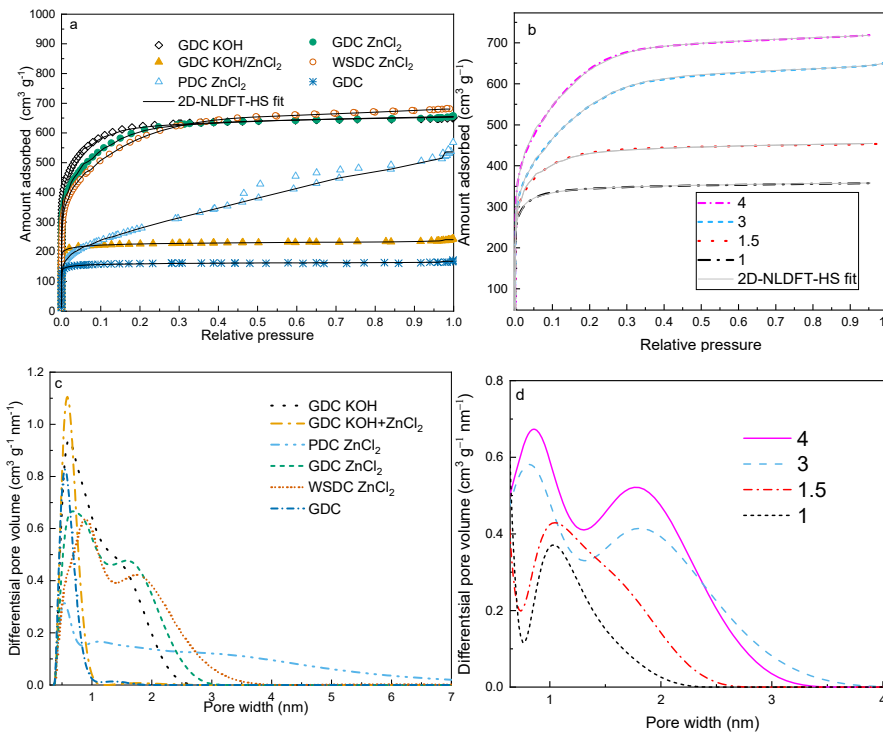

Figure 12. Experimental N_2 isotherms for different carbon materials (a) and GDC $ZnCl_2$ activation related to varying activating agent mass rations (b). PSD for different activated carbon materials (c) and PSD for GDC $ZnCl_2$ activation by varying activating agent mass ratios (noted in Figure) (d) based on the 2D-NLDFT model.

Table 1. Porosity parameters for synthesized carbon materials.

Carbon material	S_{BET} / $m^2\ g^{-1}$	V_{tot} / $cm^3\ g^{-1}$	S_{DFT} / $m^2\ g^{-1}$	V_{DFT} / $cm^3\ g^{-1}$
GDC (no activation)	540	0.26	840	0.26
GDC $ZnCl_2$ (1:1)	1210	0.55	1530	0.54
GDC $ZnCl_2$ (1:1.5)	1820	0.84	1590	0.66
GDC $ZnCl_2$ (1:3)	1990	0.96	1470	0.91
GDC $ZnCl_2$ (1:4)	2320	1.01	1700	1.01
GDC KOH (1:4)	2150	1.00	1990	0.93
GDC KOH/$ZnCl_2$ (1:2:2)	750	0.37	1120	0.36
GDC $ZnCl_2$ (1:4)	2150	1.01	1740	0.92
PDC $ZnCl_2$ (1:4)	1000	0.83	840	0.78
WSDC $ZnCl_2$ (1:4)	2110	1.05	1600	0.96

S_{BET} – specific surface area is calculated according to the BET theory, V_{tot} – total volume of pores is calculated from the adsorbed amount near the saturation pressure, S_{DFT} – and V_{DFT} – specific surface area and total pore volume, respectively, are calculated with the 2D-NLDFT-HS model using the SAIEUS software.

6.2 Electrochemical characterization

6.2.1 Cyclic voltammetry results

To visualize the faradaic and non-faradaic electrochemical processes near-maximum cell potential, a CV measurement was carried out. The curves presented (Fig. 13) were measured at the 3rd cycle. It was found that at smaller scan rate values (Fig. 13a,d) the test cells exhibit nearly rectangular behaviour. At higher potential scan rates noticeable deviations near maximum cell potential values have been observed. The ideal rectangular shape gradually changes as the cell resistance has more impact at higher sweep rates taking a heavy toll on the energy storage capabilities (Fig. 13b,c). The quantity of $ZnCl_2$ used for activations of carbonaceous powders did not change the overall CV shape in completed EDLC. The increased pore width, however, seems to improve high sweep rate characteristics as more of the total surface area can be utilized (Fig. 12b,c). On the other hand, altering activating reagents and precursor materials can change the overall transient state behaviour significantly. In general, the materials with more developed mesoporosity exhibited better CV characteristics. Based on CV behaviour, the KOH activated GDC show highest capacitance values (Table 2) and had the broadest ideal polarisable region in AN based electrolyte.

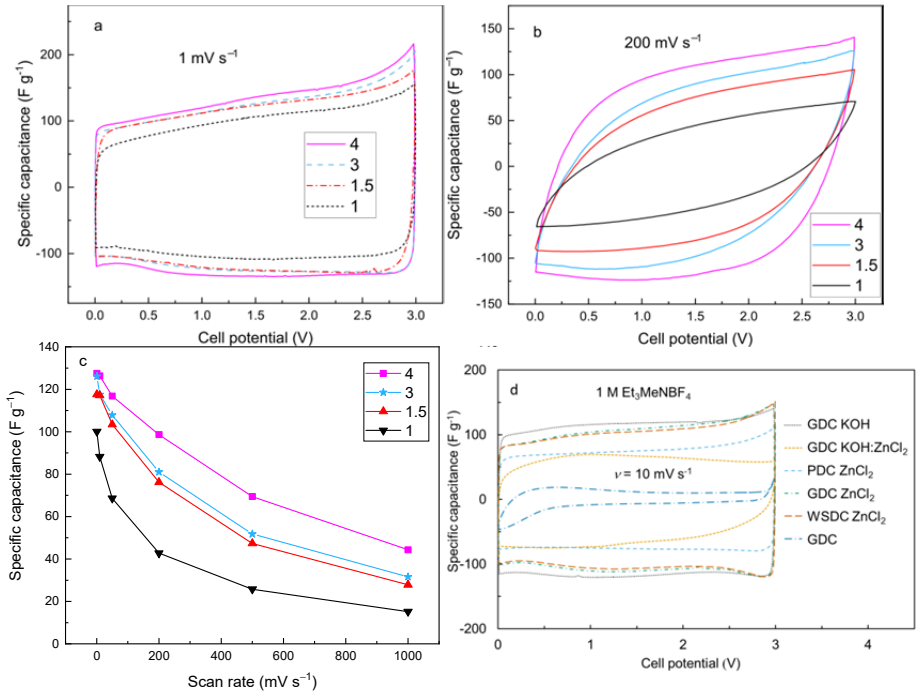

Figure 13. CV and capacitance retentions curves for GDC $ZnCl_2$ series with different activating reagent amounts (a-c) in $EMImBF_4$ electrolyte at ΔV = 3 V. CV curves for EDLC based on different activated carbon materials (d) in 1 M Et_3MeNBF_4 in AN electrolyte.

6.2.2 Constant current method results

Synthesized materials were characterized by CC method applying different fixed constant current regimes (from 0.1 to 5 A g^{-1}, Fig. 14) The discharge capacitances (Table 2), energy and coulombic efficiencies (Fig. 14) have been calculated from the data of the third charge/discharge cycle. In general, the materials with higher mesoporosity retained the ideal triangular shape even at j > 1 A g^{-1}. Calculated coulombic efficiencies (Fig. 15a) however remained constant towards change in electrode material or even the applied current density value emphasizing the questionable usefulness of this parameter toward describing the non-ideal EDLC systems. On the other hand, energy efficiencies indicated that materials with higher mesoporosity were able to maintain superior properties even at rapid transient conditions (Fig. 15a,b). This was especially apparent for AN based systems.

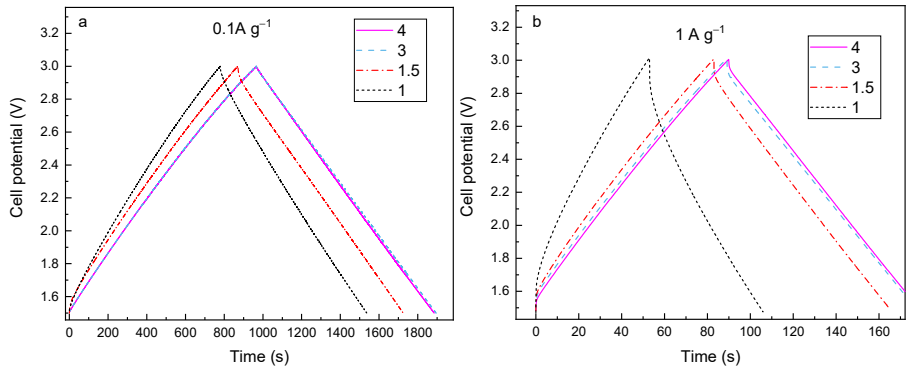

Figure 14. Constant current charge/discharge cycles at current density j = 0.1 A g^{-1} (a) and j = 1 A g^{-1} (b) in $EMImBF_4$ electrolyte for different activated carbons ($ZnCl_2$ amount noted in the figure).

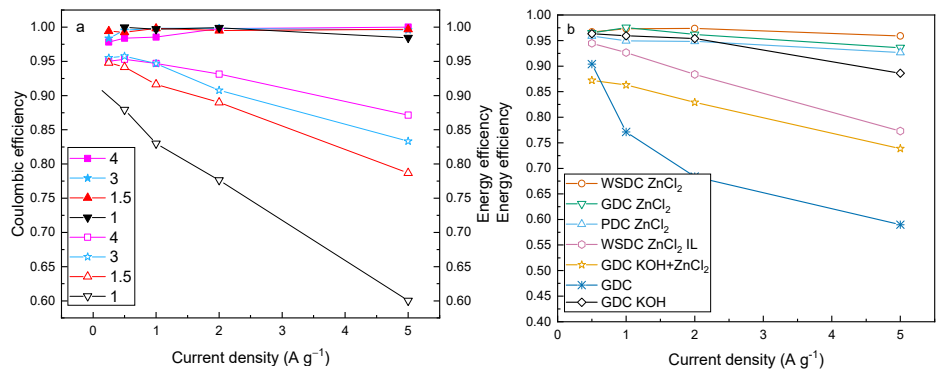

Figure 15. Columbic (filled symbols) and energy efficiencies (empty symbols) vs current density plots for vairing $ZnCl_2$ amounts (noted in figure) for GDC series in 1 M Et_3MeNBF_4 in AN electrolyte (a) and for different activated carbons (b)(noted in figure) in 1 M Et_3MeNBF_4 in AN and $EMImBF_4$ (WSDC $ZnCl_2$) electrolyte.

6.2.3 Electrochemical impedance spectroscopy results

Experimental Nyquist plots were measured in the two-electrode cell at fixed cell potentials using 5 mV perturbation amplitude. Fig. 16 shows the impact of different materials for 1 M Et_3MeNBF_4 in AN based EDLC performance. At cell potential 3 V, the materials exhibit almost linear low-frequency behaviour, where two materials with lower porosity (GDC and GDC KOH+$ZnCl_2$) show some residual frequency dependency even at 1 mV. At such sluggish perturbation, all the surface is active meaning that these two materials exhibit slow faradaic reactions and cannot be used at so high cell potential.

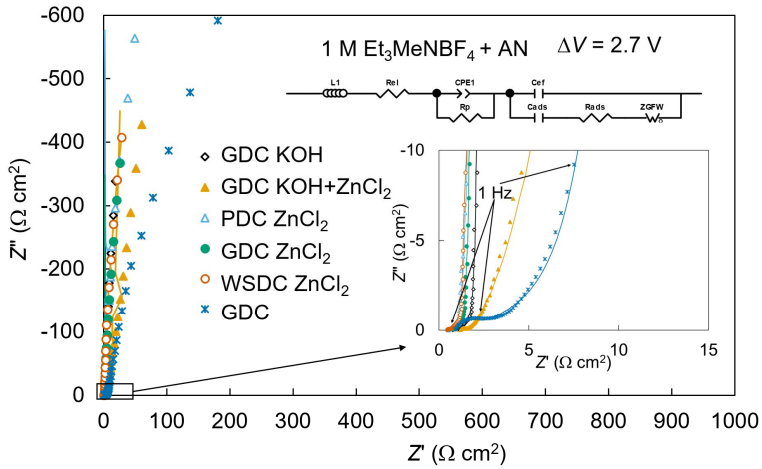

Figure 16. Nyquist plots for the EDLCs based on the different carbon material (symbols, noted in the figure) and fit results (line) in 1 M Et_3MeNBF_4 in AN electrolyte. The equivalent circuit used for fitting is given in inset of figure.

Synthesized materials that were systematically tested in $EMImBF_4$ and 1 M Et_3MeNBF_4 in AN based electrolytes showed drastic differences in the high to the middle-frequency region (Fig. 17). The IL-based systems had roughly three times higher R_{ES} values compared to AN based EDLC. The IL-based system also had a considerably wider diffusion controlled region. This can be explained by the bulk electrolyte physical properties, where IL electrolyte having almost two orders higher viscosity (η_{AN} = 0.41 mPa s vs η_{IL} = 38.2 mPa s) and more than three times lower conductivity (κ_{AN} = 50.2 mS cm^{-1} vs κ_{IL} = 13.6 mS cm^{-1}) than AN based electrolytes [27].

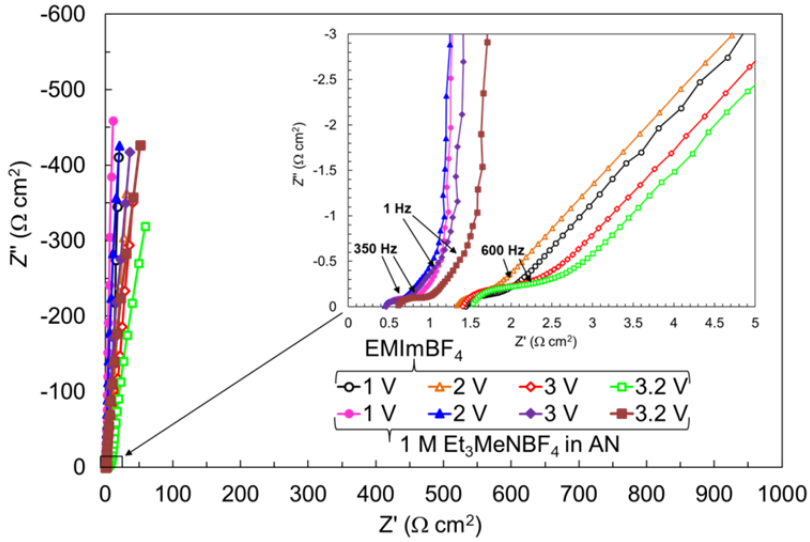

Figure 17. Nyquist plot for WSDC $ZnCl_2$ in different electrolytes in 1 M Et_3MeNBF_4 in AN (filled symbols) and $EMImBF_4$ (empty symbols) electrolyte. Applied potentials are given in the figure.

The C_s values calculated from EIS data reach plateau values as the timescale of the experiment reaches around 0.1 Hz frequencies range (Fig. 18).

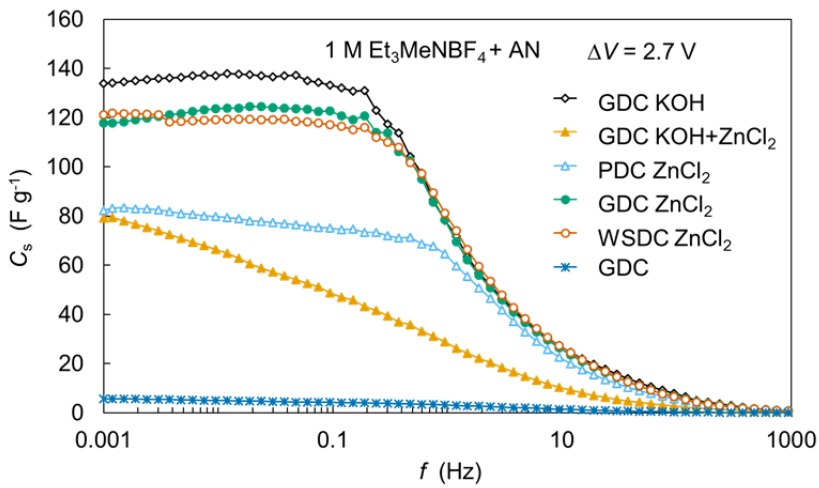

Figure 18. Specific series capacitance vs ac frequency dependencies for the EDLCs based on the different carbon materials (noted in the figure) in 1 M Et_3MeNBF_4 in AN electrolyte at $\Delta V = 2.7$ V.

The maximum series capacitance is heavily dependent on the carbon material used. The materials with higher specific surface areas have more active sites and demonstrated higher charge storage values at the same cell potentials. The capacitance values obtained from EIS measurements are backed up with the transient state studies (CC and CV data, Table 2) that provide similar results.

Besides capacitance values, systems specific characteristic time constant (τ_{char}) values were calculated by fitting the low-frequency C'' peak areas with a polynomial and interpolating the maximum value. Theses τ_{char} correspond to the "knee" frequency, where the perturbation signal triggers the whole usable surface. Surprisingly, the shortest τ_{char} values were obtained for materials with the lowest mesoporosity (Fig. 19, Table 1). Most likely, for these materials, the active surface does not include the pore depths of carbon particles, simplifying the mass transport loop. However, materials with reasonable mesoporosity also showed short τ_{char} values (under 1 s) in AN based electrolytes. In $EMImBF_4$ electrolyte, the same materials had several times higher τ_{char} values (Table 2) due to mass transport limitation in a more viscous medium.

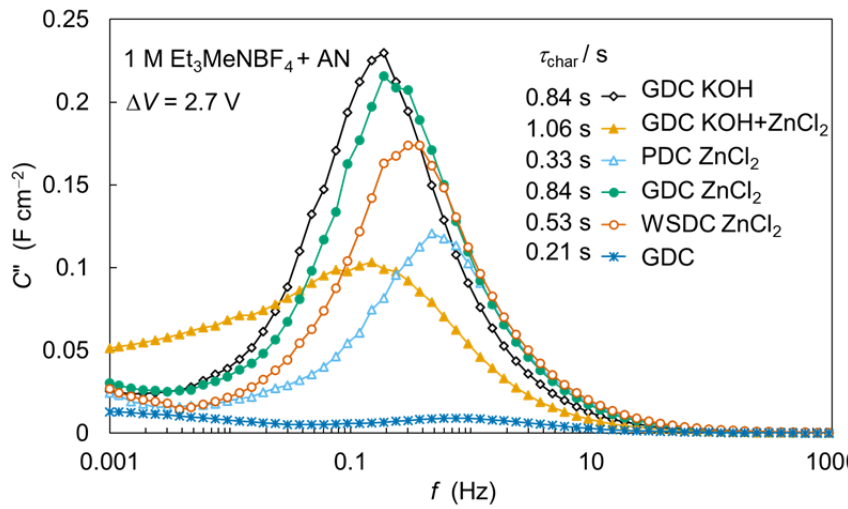

Figure 19. The imaginary part of capacitance vs ac frequency plots for the EDLCs based on the different carbon materials (noted in the figure).

Table 2. Calculated capacitance and characteristic time constant values.

Carbon material	Electrolyte	C_{CV} (F g^{-1})	C_{CC} (F g^{-1})	C_s (F g^{-1})	τ_{char} (s)
GDC KOH	Et_3MeNBF_4 in AN	131	136	134	0.84
GDC KOH+ $ZnCl_2$	Et_3MeNBF_4 in AN	77	57	79	1.06
GDC $ZnCl_2$	Et_3MeNBF_4 in AN	112	108	118	0.84
PDC $ZnCl_2$	Et_3MeNBF_4 in AN	80	77	83	0.33
WSDC $ZnCl_2$	Et_3MeNBF_4 in AN	110	109	121	0.53
GDC	Et_3MeNBF_4 in AN	19	5	6	0.21
WSDC $ZnCl_2$	$EMImBF_4$	134	136	141	4.21
GDC $ZnCl_2$	$EMImBF_4$	128	123	140	2.12

C_{CV} – specific capacitance, calculated from CV curves within the cell potential range from 0 to 3.0 V using the integrated charge Q obtained at potential scan rate v = 1 mV s^{-1}; C_{DC} – average specific capacitance, calculated from DC curves within the cell potential range from 1.5 to 3.0 V; C_s – specific series capacitance, calculated from electrochemical impedance data at cell potential ΔV = 3.0 V. τ_{char} – characteristic time constant, calculated from C'' vs f plots at maximum frequency values.

6.2.3.1 EIS fitting

EIS data shown in Fig. 16 were fitted with the same equivalent circuit (EC) (shown in the graph) to compare different materials in detail.

Table 3. Fitting results.

	R_p / Ω cm^2	C_{ef} / μF cm^{-2}	C_{ads} / F cm^{-2}	R_{ads} / Ω cm^2
WSDC $ZnCl_2$ AN	1.39 ± 0.13	217 ± 20	0.3902 ± 0.0018	0.111 ± 0.074
PDC $ZnCl_2$ AN	3.5 ± 1.9	219 ± 51	0.2762 ± 0.0016	0.05706 ± 0.0097
GDC $ZnCl_2$ AN	1.72 ± 0.25	331 ± 2.5	0.4667 ± 0.0030	0.1746 ± 0.0078
GDC KOH AN	1.29 ± 0.10	19.19 ± 0.92	0.4836 ± 0.0024	0.3810 ± 0.0088
GDC KOH $ZnCl_2$ AN	12 ± N/A	11.6 ± 0.7	0.285 ± 0.004	0.488 ± 0.012
GDC AN	5.6 ± 1.2	53 ± 21	0.0600 ± 0.0062	0.49 ± 0.13
WSDC $ZnCl_2$ IL	14.07 ± 0.94	103 ± 10	0.4869 ± 0.0045	0.289 ± 0.015

In the EC, L – the high-frequency (wire) inductance, C_{ef} – "true" interfacial capacitance (without adsorption effects), C_{ads} – the adsorption capacitance and R_{ads} – the adsorption resistance. R_p – the parallel resistance, which describes the high-frequency behaviour.

Prior to fitting, Kramers–Kronig analysis was carried out on EIS data to determine the suitable frequency range, resulting in some low-frequency points being discarded. The best fit was obtained with an equivalent circuit model that consisted of eight elements in total [80,81]. The same EC model was applied both AN and IL-based EDLC systems. Our fitting results revealed that the C_{ads} values are more than three orders greater than C_{ef} values for both electrolytes (Table 3). This means that the low frequency series resistance $C_s(f\rightarrow 0)$ is mainly dominated by the slow adsorption of electrolytic ions onto/into the porous

electrode surface. It is also apparent that R_{ads} values are lower for material with higher mesoporosity due to having a more developed mass-transport network.

6.2.4 Constant power measurements

For more variable load electrochemical characteristics of the electrode materials, constant power (CP) test at cell potential range from 3 V to 1.5 V was performed.

In general, the power/energy characteristics were found highly dependent on the electrode material used. For similar materials, changing the 1M Et_3MeNBF_4 in AN electrolyte to $EMImBF_4$ (IL) improved the maximum specific energy achieved, but on the other hand, this exchange also resulted in reduced maximum specific power values (Fig. 20). Additionally, the activated carbons with high mesoporosity showed significantly better power and energy characteristics compared materials that are almost entirely microporous.

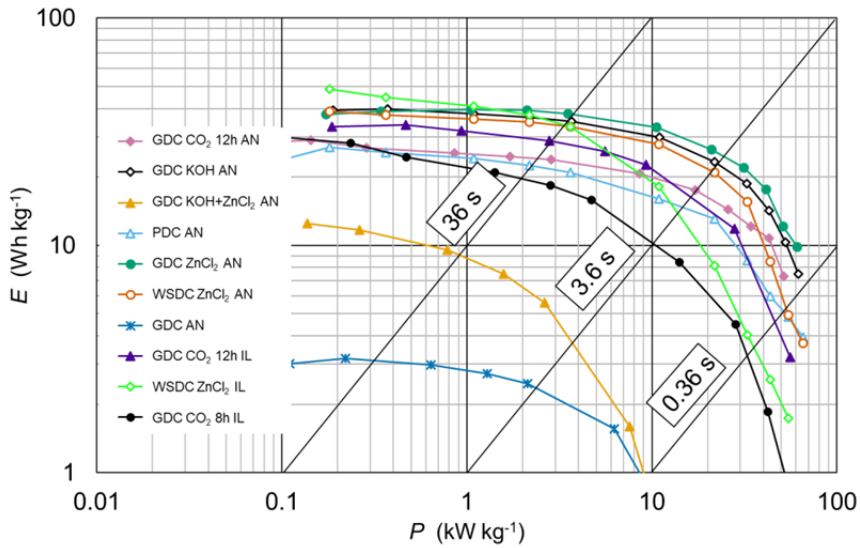

Figure 20. Ragone plots for EDLC based on different materials (noted in the figure) filled with IL ($EMImBF_4$) or 1M Et_3MeNBF_4 in AN electrolyte (noted in the figure).

For more detailed analysis, a total of 36 carbide-derived and sugar-derived carbons was included to assess the key parameters for high power EDLC [10,81]. As a first approximation method, correlations with the pore length obtained by 2D NDLFT model (around electrolyte ion cross-section length) to the specific power values at 0.36 s (Fig. 21) and 3.6 s (Fig. 22) were constructed. Despite the simplistic approach, the correlation coefficients (noted in the figure) show interesting trends describing the pores contributing to expe-

rimental power characteristics. Based on the statistical results in Figs. 21 and 22, the pore width strongly influenced the power characteristic of the carbon materials. To assess linear and nonlinear cases, the experimental correlation Pearson's and Spearman's correlation coefficients were calculated. Both correlation coefficients increase with the increase of the pore widths. When the discharge time was increased from 0.36 s to 3.6 s the mass transport to smaller pores was made possible and the corresponding correlation coefficients along with power values also increased. It was observed that pores smaller than 0.85 nm have a questionable contribution on adsorption processes at the timescale of 3.6 s and below. It is possible that at longer time intervals, the pores under 0.85 nm will show meaningful correlations, but then the EDLC studied will lose their core functions as a high power device.

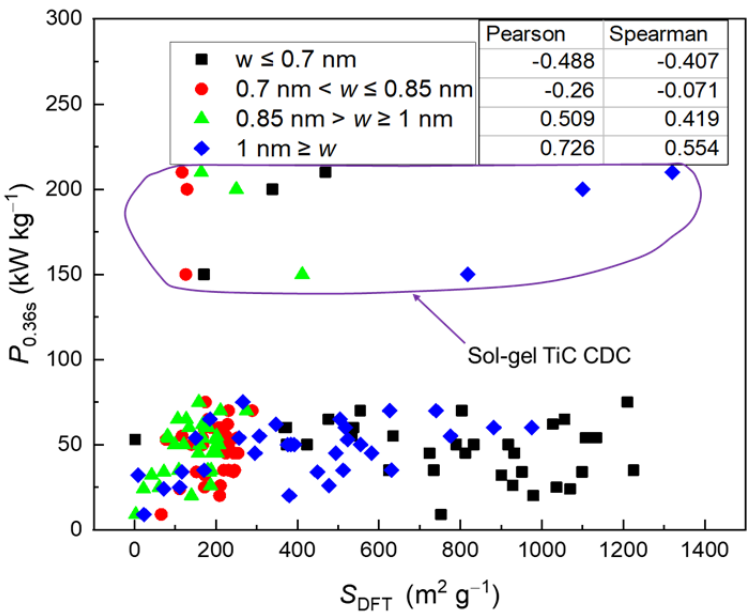

Figure 21. Correlation data between carbon materials pore surface areas at varying pore widths vs specific power of EDLC based on the same carbon material at 0.36 s discharge time in Et_3MeNBF_4 in AN electrolyte.

At pore width over 0.85 nm, correlations with $P_{0.36s}$ rapidly turns positive and the correlation coefficients seem to increase as wider pore widths are compared. Thus, it seems that pore widths above 0.85 nm are very crucial for high power devices electrode materials.

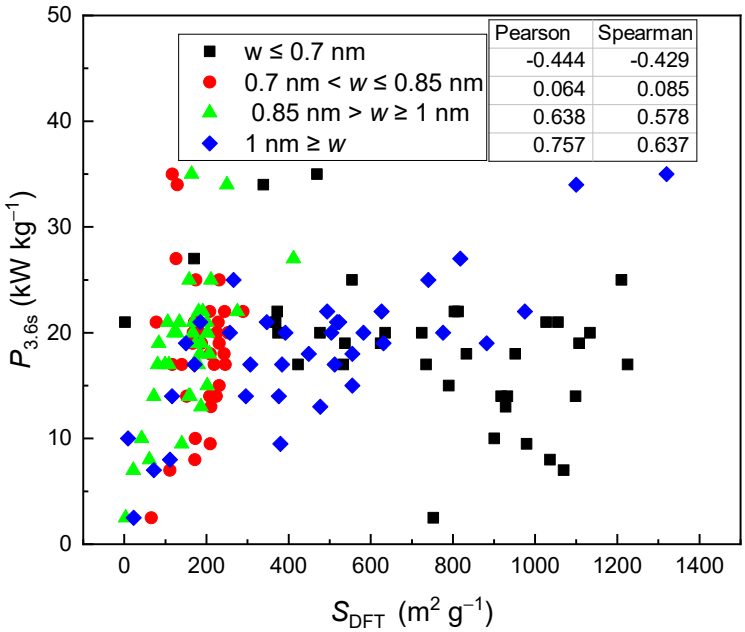

Figure 22. Correlation data between carbon materials pore surface areas at varying pore widths vs specific power of EDLC based on the same carbon material at 3.6 s discharge time in Et_3MeNBF_4 in AN electrolyte.

7. SUMMARY

Several activated carbons with different porosities were synthesized via a novel two-step process using hydrothermal carbonization and subsequent activation steps. The physical parameters of the activated carbon materials have been analyzed and compared to the results obtained by the electrochemical measurements to improve EDLC applications further.

Based on the XRD and Raman spectroscopy results, the obtained materials lack well ordered crystalline structures and are highly disordered. The KOH activation did, however, produce more disordered carbons and changed the initial carbon more, in comparison to the $ZnCl_2$ activation, which did not alter the carbon structure noticeably. The SEM images visualized the effects of fundamentally different surface reactions occurring during KOH and $ZnCl_2$ activations, but both reagents surprisingly caused rather similar porosity development in the carbon structure. The gas sorption analysis data also revealed the porous structure that can be tailored further to match the need by altering the initial quantity of the activating reagent.

The two-electrode symmetrical test cells were completed using the synthesized carbon materials and $EMImBF_4$ ionic liquid or Et_3MeNBF_4 in AN were used as the electrolytes. The shapes of the measured EIS, CV, CC and CP curves were highly dependent on the activated carbon electrodes as the EDL is formed at and in the vicinity of the electrode surface.

The EIS and CV measurements results indicated that the best materials can be successfully used at cell potential up to 3 V. Also EIS revealed that lower characteristic time constant values were calculated for materials with almost no mesoporosity and for materials with the highest mesoporosity giving the impression that highly microporous materials do not fully use their available surface area. This was also observed through the statistical analysis of experimental power and pore width correlations which revealed the critical role of pores over 0.85 nm in width for completing high power EDLCs.

Systematic analysis of data collected shows that from all of the synthesized materials the best energy storage properties were observed for GDC KOH and GDC $ZnCl_2$, where four-times more activating reagent was used compared to the carbonaceous precursor. All the activating reagents successfully increased the porosity (reaching up to S_{DFT} = 1990 $m^2\ g^{-1}$) resulting in high measured power density (P_{max} = 60 kW kg^{-1}) devices that maintained reasonably high energy densities (E =10 W h kg^{-1}). With the IL electrolyte slightly higher maximum energy (48 W h kg^{-1}) and capacitance (140 F g^{-1}) values were achieved. However, as a drawback, the use of IL lowered capacitance retention and maximum power values. In conclusion, activated carbon obtained via the HTC process produce very interesting electrode materials for EDLC applications, but there is some room for improvements to meet ambitious industry requirements.

8. REFERENCES

[1] C. Schütter, S. Pohlmann, A. Balducci, Industrial Requirements of Materials for Electrical Double Layer Capacitors: Impact on Current and Future Applications, Adv. Energy Mater. 9 (2019) 1900334. https://doi.org/10.1002/aenm.201900334.

[2] J. Krummacher, C. Schütter, L.H. Hess, A. Balducci, Non-aqueous electrolytes for electrochemical capacitors, Curr. Opin. Electrochem. 9 (2018) 64–69. https://doi.org/10.1016/j.coelec.2018.03.036.

[3] E.E. Miller, Y. Hua, F.H. Tezel, Materials for energy storage: Review of electrode materials and methods of increasing capacitance for supercapacitors, J. Energy Storage. 20 (2018) 30–40. https://doi.org/10.1016/j.est.2018.08.009.

[4] Z. Lin, E. Goikolea, A. Balducci, K. Naoi, P.L. Taberna, M. Salanne, G. Yushin, P. Simon, Materials for supercapacitors: When Li-ion battery power is not enough, Mater. Today. 21 (2018) 419–436. https://doi.org/10.1016/j.mattod.2018.01.035.

[5] H. Ji, X. Zhao, Z. Qiao, J. Jung, Y. Zhu, Y. Lu, L.L. Zhang, A.H. MacDonald, R.S. Ruoff, Capacitance of carbon-based electrical double-layer capacitors, Nat. Commun. 5 (2014) 1–7. https://doi.org/10.1038/ncomms4317.

[6] T. Kuila, S. Bose, A.K. Mishra, P. Khanra, N.H. Kim, J.H. Lee, Chemical functionalization of graphene and its applications, Prog. Mater. Sci. 57 (2012) 1061–1105. https://doi.org/10.1016/j.pmatsci.2012.03.002.

[7] Y. Chen, B. Zhang, G. Liu, X. Zhuang, E.-T. Kang, Graphene and its derivatives: switching ON and OFF, Chem. Soc. Rev. 41 (2012) 4688–4707. https://doi.org/10.1039/C2CS35043B.

[8] R.M. Dell, D.A.J. Rand, Clean Energy, Royal Society of Chemistry, 2007.

[9] G. Wang, L. Zhang, J. Zhang, A review of electrode materials for electrochemical supercapacitors, Chem. Soc. Rev. 41 (2012) 797–828. https://doi.org/10.1039/C1CS15060J.

[10] R. Härmas, R. Palm, M. Härmas, M. Pohl, H. Kurig, I. Tallo, E. Tee, I. Vaas, R. Väli, T. Romann, O. Oll, R. Kanarbik, K. Liivand, J. Eskusson, J. Kruusma, T. Thomberg, A. Jänes, P. Miidla, E. Lust, Influence of porosity parameters and electrolyte chemical composition on the power densities of non-aqueous and ionic liquid based supercapacitors, Electrochimica Acta. 283 (2018) 931–948. https://doi.org/10.1016/j.electacta.2018.06.115.

[11] A.M. Abioye, F.N. Ani, Recent development in the production of activated carbon electrodes from agricultural waste biomass for supercapacitors: A review, Renew. Sustain. Energy Rev. 52 (2015) 1282–1293. https://doi.org/10.1016/j.rser.2015.07.129.

[12] A.K. Samantara, S. Ratha, Materials Development for Active/Passive Components of a Supercapacitor, Springer, 2018.
https://doi.org/10.1007/978-981-10-7263-5

[13] S. Kulandaivalu, Y. Sulaiman, Recent Advances in Layer-by-Layer Assembled Conducting Polymer Based Composites for Supercapacitors, Energies. 12 (2019) 2107. https://doi.org/10.3390/en12112107.

[14] R. Kötz, M. Carlen, Principles and applications of electrochemical capacitors, Electrochimica Acta. 45 (2000) 2483–2498. https://doi.org/10.1016/S0013-4686(00)00354-6.

[15] S. Ratha, A.K. Samantara, Supercapacitor: Instrumentation, Measurement and Performance Evaluation Techniques, 1st ed., Springer, 2018.

[16] T. Brousse, D. Bélanger, J.W. Long, To Be or Not To Be Pseudocapacitive?, J. Electrochem. Soc. 162 (2015) A5185–A5189. https://doi.org/10.1149/2.0201505jes.
[17] F. Beguin, E. Frackowiak, Supercapacitors: Materials, Systems and Applications, John Wiley & Sons, 2013.
[18] CRC Handbook of Chemistry and Physics, 2009−2010, 90th ed., J. Am. Chem. Soc. 131 (2009) 12862–12862. https://doi.org/10.1021/ja906434c.
[19] D. Dasgupta, F. Demichelis, A. Tagliaferro, Electrical conductivity of amorphous carbon and amorphous hydrogenated carbon, Philos. Mag. B. 63 (1991) 1255–1266. https://doi.org/10.1080/13642819108205558.
[20] C.J. Adkins, S.M. Freake, E.M. Hamilton, Electrical conduction in amorphous carbon, Philos. Mag. J. Theor. Exp. Appl. Phys. 22 (1970) 183–188. https://doi.org/10.1080/14786437008228163.
[21] C. Zhong, Y. Deng, W. Hu, J. Qiao, L. Zhang, J. Zhang, A review of electrolyte materials and compositions for electrochemical supercapacitors, Chem. Soc. Rev. 44 (2015) 7484–7539. https://doi.org/10.1039/C5CS00303B.
[22] A. Burke, M. Miller, The power capability of ultracapacitors and lithium batteries for electric and hybrid vehicle applications, J. Power Sources. 196 (2011) 514–522. https://doi.org/10.1016/j.jpowsour.2010.06.092.
[23] L. Chen, H. Bai, Z. Huang, L. Li, Mechanism investigation and suppression of self-discharge in active electrolyte enhanced supercapacitors, Energy Environ. Sci. 7 (2014) 1750–1759. https://doi.org/10.1039/C4EE00002A.
[24] J.M. Baptista, J.S. Sagu, U.W. Kg, K. Lobato, State-of-the-art materials for high power and high energy supercapacitors: Performance metrics and obstacles for the transition from lab to industrial scale – A critical approach, Chem. Eng. J. 374 (2019) 1153–1179. https://doi.org/10.1016/j.cej.2019.05.207.
[25] F. Jin, ed., Application of Hydrothermal Reactions to Biomass Conversion, Springer-Verlag, Berlin Heidelberg, 2014. https://doi.org/10.1007/978-3-642-54458-3.
[26] K.H. Adolfsson, N. Yadav, M. Hakkarainen, Cellulose-Derived Hydrothermally Carbonized Materials and Their Emerging Applications, Curr. Opin. Green Sustain. Chem. 23 (2020) 18–24. https://doi.org/10.1016/j.cogsc.2020.03.008.
[27] M. Härmas, T. Thomberg, T. Romann, A. Jänes, E. Lust, Carbon for Energy Storage Derived from Granulated White Sugar by Hydrothermal Carbonization and Subsequent Zinc Chloride Activation, J. Electrochem. Soc. 164 (2017) A1866–A1872. https://doi.org/10.1149/2.0681709jes.
[28] M. Heidari, A. Dutta, B. Acharya, S. Mahmud, A review of the current knowledge and challenges of hydrothermal carbonization for biomass conversion, J. Energy Inst. 92 (2019) 1779–1799. https://doi.org/10.1016/j.joei.2018.12.003.
[29] M. Uematsu, E.U. Frank, Static Dielectric Constant of Water and Steam, J. Phys. Chem. Ref. Data. 9 (1980) 1291–1306. https://doi.org/10.1063/1.555632.
[30] M.-M. Titirici, R.J. White, C. Falco, M. Sevilla, Black perspectives for a green future: hydrothermal carbons for environment protection and energy storage, Energy Environ. Sci. 5 (2012) 6796–6822. https://doi.org/10.1039/C2EE21166A.
[31] J.N. Chheda, Y. Román-Leshkov, J.A. Dumesic, Production of 5-hydroxymethylfurfural and furfural by dehydration of biomass-derived mono- and poly-saccharides, Green Chem. 9 (2007) 342–350. https://doi.org/10.1039/B611568C.

[32] M. Sevilla, A.B. Fuertes, Chemical and Structural Properties of Carbonaceous Products Obtained by Hydrothermal Carbonization of Saccharides, Chem. – Eur. J. 15 (2009) 4195–4203. https://doi.org/10.1002/chem.200802097.
[33] A.J. Romero-Anaya, M. Ouzzine, M.A. Lillo-Ródenas, A. Linares-Solano, Spherical carbons: Synthesis, characterization and activation processes, Carbon. 68 (2014) 296–307. https://doi.org/10.1016/j.carbon.2013.11.006.
[34] M. Käärik, M. Arulepp, M. Käärik, U. Maran, J. Leis, Characterization and prediction of double-layer capacitance of nanoporous carbon materials using the Quantitative nano-Structure-Property Relationship approach based on experimentally determined porosity descriptors, Carbon. 158 (2020) 494–504. https://doi.org/10.1016/j.carbon.2019.11.017.
[35] H. Marsh, F.R. Reinoso, Activated Carbon, Elsevier, 2006.
[36] J.A. Maciá-Agulló, B.C. Moore, D. Cazorla-Amorós, A. Linares-Solano, Activation of coal tar pitch carbon fibres: Physical activation vs. chemical activation, Carbon. 42 (2004) 1367–1370. https://doi.org/10.1016/j.carbon.2004.01.013.
[37] R. Xiong, Y. Zhang, W. Zhou, K. Xia, Q. Sun, G. Chen, B. Han, Q. Gao, C. Zhou, Chemical activation of carbon materials for supercapacitors: Elucidating the effect of spatial characteristics of the precursors, Colloids Surf. Physicochem. Eng. Asp. 597 (2020) 124762. https://doi.org/10.1016/j.colsurfa.2020.124762.
[38] M.A. Lillo-Ródenas, J. Juan-Juan, D. Cazorla-Amorós, A. Linares-Solano, About reactions occurring during chemical activation with hydroxides, Carbon. 42 (2004) 1371–1375. https://doi.org/10.1016/j.carbon.2004.01.008.
[39] M. Molina-Sabio, F. Rodriguez-Reinoso, Role of chemical activation in the development of carbon porosity, Colloids Surf. A Physicochem. Eng. Asp. 241 (2004) 15–25. https://doi.org/10.1016/j.colsurfa.2004.04.007.
[40] H. Teng, H.-C. Lin, H. Teng, Activated carbon production from low ash subbituminous coal with CO_2 activation, AIChE J. 44 (1998) 1170–1177. https://doi.org/10.1002/aic.690440514.
[41] A. Jain, R. Balasubramanian, M.P. Srinivasan, Hydrothermal conversion of biomass waste to activated carbon with high porosity: A review, Chem. Eng. J. 283 (2016) 789–805. https://doi.org/10.1016/j.cej.2015.08.014.
[42] R. Khoshbouy, F. Takahashi, K. Yoshikawa, Preparation of high surface area sludge-based activated hydrochar via hydrothermal carbonization and application in the removal of basic dye, Environ. Res. 175 (2019) 457–467. https:// doi.org/10.1016/j.envres.2019.04.002.
[43] T. Wang, Y. Zhai, Y. Zhu, C. Li, G. Zeng, A review of the hydrothermal carbonization of biomass waste for hydrochar formation: Process conditions, fundamentals, and physicochemical properties, Renew. Sustain. Energy Rev. 90 (2018) 223–247. https://doi.org/10.1016/j.rser.2018.03.071.
[44] C. Dai, J. Wan, J. Yang, S. Qu, T. Jin, F. Ma, J. Shao, H_3PO_4 solution hydrothermal carbonization combined with KOH activation to prepare argy wormwood-based porous carbon for high-performance supercapacitors, Appl. Surf. Sci. 444 (2018) 105–117. https://doi.org/10.1016/j.apsusc.2018.02.261.
[45] M. Härmas, T. Thomberg, H. Kurig, T. Romann, A. Jänes, E. Lust, Microporous–mesoporous carbons for energy storage synthesized by activation of carbonaceous material by zinc chloride, potassium hydroxide or mixture of them, J. Power Sources. 326 (2016) 624–634. https://doi.org/10.1016/j.jpowsour.2016.04.038.

[46] M. Härmas, T. Thomberg, A. Jänes, Effect of Zinc Chloride Activation on D-Glucose Derived Carbons Based Capacitors Performance in Ionic Liquid, J. Electrochem. Soc. 167 (2020) 080533. https://doi.org/10.1149/1945-7111/ab8ecf.
[47] L. Wei, M. Sevilla, A.B. Fuertes, R. Mokaya, G. Yushin, Hydrothermal Carbonization of Abundant Renewable Natural Organic Chemicals for High-Performance Supercapacitor Electrodes, Adv. Energy Mater. 1 (2011) 356–361. https://doi.org/10.1002/aenm.201100019.
[48] C. Falco, J. Marco-Lozar, D. Salinas-Torres, E. Morallon, D. Cazorla-Amoros, M. Titirici, D. Lozano-Castello, Tailoring the porosity of chemically activated hydrothermal carbons: Influence of the precursor and hydrothermal carbonization temperature, Carbon. 62 (2013) 346–355.
[49] E. Gonzalez-Serrano, T. Cordero, J. Rodríguez-Mirasol, J.J. Rodríguez, Development of Porosity upon Chemical Activation of Kraft Lignin with $ZnCl_2$, Ind. Eng. Chem. Res. 36 (1997) 4832–4838.
[50] M.A. Lillo-Ródenas, D. Cazorla-Amorós, A. Linares-Solano, Understanding chemical reactions between carbons and NaOH and KOH: An insight into the chemical activation mechanism, Carbon. 41 (2003) 267–275. https://doi.org/10.1016/S0008-6223(02)00279-8.
[51] D. Lozano-Castelló, M.A. Lillo-Ródenas, D. Cazorla-Amorós, A. Linares-Solano, Preparation of activated carbons from Spanish anthracite: I. Activation by KOH, Carbon. 39 (2001) 741–749. https://doi.org/10.1016/S0008-6223(00)00185-8.
[52] B.E. Conway, Electrochemical supercapacitors: scientific fundamentals and technological applications, Springer, New York, 1999.
[53] A.J. Bard, L.R. Faulkner, Electrochemical Methods: Fundamentals and Applications 2nd ed., N. Y. Wiley. 38 (2002) 1364–1365. https://doi.org/10.1023/A:1021637209564.
[54] A. Laheäär, P. Przygocki, Q. Abbas, F. Béguin, Appropriate methods for evaluating the efficiency and capacitive behavior of different types of supercapacitors, Electrochem. Commun. 60 (2015) 21–25. https://doi.org/10.1016/j.elecom.2015.07.022.
[53] E. Barsoukov, J.R. Macdonald, Impedance Spectroscopy: Theory, Experiment, and Applications, 2nd ed., 2005.
[56] H.-K. Song, H.-Y. Hwang, K.-H. Lee, L.H. Dao, The effect of pore size distribution on the frequency dispersion of porous electrodes, Electrochimica Acta. 45 (2000) 2241–2257. https://doi.org/10.1016/S0013-4686(99)00436-3.
[57] H. Keiser, K.D. Beccu, M.A. Gutjahr, Abschätzung der porenstruktur poröser elektroden aus impedanzmessungen, Electrochimica Acta. 21 (1976) 539–543. https://doi.org/10.1016/0013-4686(76)85147-X.
[58] R.C. Bansal, M. Goyal, Activated Carbon Adsorption, CRC Press, 2005.
[59] M. Thommes, K. Kaneko, A.V. Neimark, J.P. Olivier, F. Rodriguez-Reinoso, J. Rouquerol, K.S.W. Sing, Physisorption of gases, with special reference to the evaluation of surface area and pore size distribution (IUPAC Technical Report), Pure Appl. Chem. 87 (2015) 1051–1069. https://doi.org/10.1515/pac-2014-1117.
[60] K.S.W. Sing, Reporting physisorption data for gas/solid systems with special reference to the determination of surface area and porosity (Recommendations 1984), Pure Appl. Chem. 57 (1985) 603–619. https://doi.org/10.1351/ pac198557040603.
[61] S. Lowell, J.E. Shields, M.A. Thomas, M. Thommes, Characterization of Porous Solids and Powders: Surface Area, Pore Size and Density, 4th Revised edition, Springer, Dordrecht ; Boston, 2004.

[62] A.M. Puziy, O.I. Poddubnaya, B. Gawdzik, M. Sobiesiak, Comparison of heterogeneous pore models QSDFT and 2D-NLDFT and computer programs ASiQwin and SAIEUS for calculation of pore size distribution, Adsorption. 22 (2016) 459–464. https://doi.org/10.1007/s10450-015-9704-6.
[63] J.A. Libra, K.S. Ro, C. Kammann, A. Funke, N.D. Berge, Y. Neubauer, M.-M. Titirici, C. Fühner, O. Bens, J. Kern, K.-H. Emmerich, Hydrothermal carbonization of biomass residuals: a comparative review of the chemistry, processes and applications of wet and dry pyrolysis, Biofuels. 2 (2011) 71–106. https://doi.org/10.4155/bfs.10.81.
[64] S.K. Hoekman, A. Broch, C. Robbins, B. Zielińska, L.G. Felix, Hydrothermal carbonization (HTC) of selected woody and herbaceous biomass feedstocks, Biomass Convers. Biorefin. 3 (2013) 113–126. https://doi.org/10.1007/s13399-012-0066-y.
[65] K. Aydıncak, T. Yumak, A. Sınağ, B. Esen, Synthesis and Characterization of Carbonaceous Materials from Saccharides (Glucose and Lactose) and Two Waste Biomasses by Hydrothermal Carbonization, Ind. Eng. Chem. Res. 51 (2012) 9145–9152. https://doi.org/10.1021/ie301236h.
[66] M.T. Reza, M.H. Uddin, J.G. Lynam, S.K. Hoekman, C.J. Coronella, Hydrothermal carbonization of loblolly pine: reaction chemistry and water balance, Biomass Convers. Biorefinery. 4 (2014) 311–321. https://doi.org/10.1007/s13399-014-0115-9.
[67] F. Tuinstra, J.L. Koenig, Raman Spectrum of Graphite, J. Chem. Phys. 53 (1970) 1126–1130. https://doi.org/10.1063/1.1674108.
[68] A.C. Ferrari, J. Robertson, Resonant Raman spectroscopy of disordered, amorphous, and diamondlike carbon, Phys. Rev. B. 64 (2001) 075414. https://doi.org/10.1103/PhysRevB.64.075414.
[69] I. Tallo, T. Thomberg, H. Kurig, K. Kontturi, A. Jänes, E. Lust, Novel micro-mesoporous carbon materials synthesized from tantalum hafnium carbide and tungsten titanium carbide, Carbon. 67 (2014) 607–616. https://doi.org/10.1016/j.carbon.2013.10.034.
[70] M.A. Pimenta, G. Dresselhaus, M.S. Dresselhaus, L.G. Cançado, A. Jorio, R. Saito, Studying disorder in graphite-based systems by Raman spectroscopy, Phys. Chem. Chem. Phys. 9 (2007) 1276–1290. https://doi.org/10.1039/B613962K.
[71] H. Kurig, M. Russina, I. Tallo, M. Siebenbürger, T. Romann, E. Lust, The suitability of infinite slit-shaped pore model to describe the pores in highly porous carbon materials, Carbon. 100 (2016) 617–624. https://doi.org/10.1016/j.carbon.2016.01.061.
[72] M.S. Dresselhaus, G. Dresselhaus, M. Hofmann, The big picture of Raman scattering in carbon nanotubes, Vib. Spectrosc. 45 (2007) 71–81. https://doi.org/10.1016/j.vibspec.2007.07.004.
[73] J. Jiang, R. Pachter, F. Mehmood, A.E. Islam, B. Maruyama, J.J. Boeckl, A Raman spectroscopy signature for characterizing defective single-layer graphene: Defect-induced $I(D)/I(D')$ intensity ratio by theoretical analysis, Carbon. 90 (2015) 53–62. https://doi.org/10.1016/j.carbon.2015.03.049.
[74] G.A. Zickler, B. Smarsly, N. Gierlinger, H. Peterlik, O. Paris, A reconsideration of the relationship between the crystallite size La of carbons determined by X-ray diffraction and Raman spectroscopy, Carbon. 44 (2006) 3239–3246. https://doi.org/10.1016/j.carbon.2006.06.029.

[75] J. Ribeiro-Soares, M.E. Oliveros, C. Garin, M.V. David, L.G.P. Martins, C.A. Almeida, E.H. Martins-Ferreira, K. Takai, T. Enoki, R. Magalhães-Paniago, A. Malachias, A. Jorio, B.S. Archanjo, C.A. Achete, L.G. Cançado, Structural analysis of polycrystalline graphene systems by Raman spectroscopy, Carbon. 95 (2015) 646–652. https://doi.org/10.1016/j.carbon.2015.08.020.
[76] T.W. Gräwert, D.I. Svergun, Structural Modeling Using Solution Small-Angle X-ray Scattering (SAXS), J. Mol. Biol. (2020). https://doi.org/10.1016/j.jmb.2020.01.030.
[77] P. Hildebrandt, S. Lecomte, Biochemical Applications of Raman Spectroscopy, Encycl. Spectrosc. Spectrom. Second Ed., Academic Press, Oxford, 1999.
[78] A.C. Ferrari, J. Robertson, Interpretation of Raman spectra of disordered and amorphous carbon, Phys. Rev. B. 61 (2000) 14095–14107. https://doi.org/10.1103/PhysRevB.61.14095.
[79] E. Smith, G. Dent, Modern Raman Spectroscopy: A Practical Approach, 2 edition, Wiley, Hoboken, NJ, 2019.
[80] T. Tooming, T. Thomberg, H. Kurig, A. Jänes, E. Lust, High power density supercapacitors based on the carbon dioxide activated d-glucose derived carbon electrodes and 1-ethyl-3-methylimidazolium tetrafluoroborate ionic liquid, J. Power Sources. 280 (2015) 667–677. https://doi.org/10.1016/j.jpowsour.2015.01. 157.
[81] M. Härmas, R. Palm, T. Thomberg, R. Härmas, M. Koppel, M. Paalo, I. Tallo, T. Romann, A. Jänes, E. Lust, Hydrothermal and peat-derived carbons as electrode materials for high-efficient electrical double-layer capacitors, J. Appl. Electrochem. 50 (2020) 15–32. https://doi.org/10.1007/s10800-019-01364-5.

9. SUMMARY IN ESTONIAN

Aktiveeritud süsinike mikrostruktuuri ja poorsuse mõju elektrilise kaksikkihi kondensaatorite omadustele

Elektrilise kaksikkihi kondensaatorid (EKKK) on seadmed, mida kasutatakse energiaimpulsside salvestamiseks või nende genereerimiseks. Neid rakendatakse, kui on oluline salvestada/väljastada palju energiat lühikese aja jooksul ehk oluline on saavutada suur võimsus. Veel iseloomustab EKKK muljetavaldav vastupidavus nii korduva täis- ja tühjakslaadimise (eluiga >100 000 tsüklit) kui ka ekstreemsete kasutustemperatuuride (−40 kuni 85 °C) korral. See annab EKKKle suure eelise võrreldes akude ja kütuseelementidega.

Üks tähtsamaid EKKK komponente on selle elektroodid, mis määravad paljuski kogu energiasalvesti võimekuse ja hinna. Selles töös uuriti uute ja jätkusuutlike elektroodimaterjalide sünteesimise viise ning hinnati saadud materjalide füüsikalisi ja elektrokeemilisi omadusi. Elektroodimaterjalid sünteesiti kaheetapilise meetodiga, kus esimeses etapis sünteesiti süsinikurikas materjal hüdrotermilise karboniseerimise (HTK) meetodil. HTK meetod võimaldab süsiniku sünteesimiseks kasutada laia valikut lähteaineid nt suhkruid (selles töös glükoos, sahharoos) kui ka keemilise koostise mõttes keerukamaid materjale nagu turvas. Lisaks on HTK odav ja keskonnasõbralik meetod, sest keemilise reaktsiooni lahustiks on vesi.

HTK käigus saadud tahke süsinikurikas materjal ei ole piisavalt poorne ega süsiniku pind piisavalt puhas, et seda saaks edukalt kasutada elektroodimaterjalina EKKK. Seetõttu aktiveeriti HTK kaudu saadud materjali sünteesi teises etapis, kus aktiveerimiseks kasutati kaaliumhüdroksiidi (KOH) ja tsinkkloriidi ($ZnCl_2$).

Pärast kahte sünteesietappi saadi aktiveeritud süsinik, mille eripinna väärtused olid kuni 2320 $m^2\ g^{-1}$. Saadud materjale uuriti nii röntgendifraktsiooni, Raman spektroskoopia kui ka skanneeriva elektronmikroskoopia meetoditega. Leiti, et sünteesitud aktiveeritud süsinikud olid valdavalt väga ebakorrapäralise struktuuriga. Lisaks tuvastati, et osad aktiveeritud süsinikud koosnesid ~1–2 μm suurustest sfäärilistest osakestes, mis tekkisid juba HTK protsessis. Seejuures $ZnCl_2$ aktiveerimise korral säilis algne sfääriline struktuur, kuid KOH puhul tekkisid täiesti uued augulised struktuurid.

Aktiveeritud süsinikmaterjalidega teostati elektrokeemilised mõõtmised kaheelektroodilises testrakus. Parimate materjalide erimahtuvused olid kuni 140 $F\ g^{-1}$ ning erivõimsused 60 $kW\ kg^{-1}$. Lisaks analüüsiti ka erinevate laiustega pooride panust ja rolli suure võimsuse saavutamiseks EKKK tühjaks laadimisel. Leiti, et äärmiselt tähtsad on poorid mille laius on üle 0.85 nm.

Kokkuvõttes sünteesiti ja analüüsiti mitmeid huvitava struktuuriga elektrit hästi juhtivaid odavaid ja paljulubavaid EKKK elektroodimaterjale, mille mikrostruktuuri ja poorust on võimalik lähteaine valiku ja aktiveerimise tingimustega kontrollida ja muuta.

10. ACKNOWLEDGEMENTS

First and foremost, I would like to express the deepest gratitude to my supervisors, Thomas Thomberg and Alar Jänes for being there with a wise word when times were good and most importantly when the opposite was the case. You have always pushed me to be a better me, for which I am the most grateful. Thank you for the positive attitude and your multitude of ideas. However, if not officially then effectively, there has been one additional supervisor for all of the physical- and electrochemistry students – Enn Lust. Thank you for showing all of us where enthusiasm and hard work can take a person. Thank you for your everlasting patience, and the care and love you bring in this faculty and to this scientific world. For all these years, my supervisors have provided me with everything a student could ever hope for and I am ever grateful for that.

I would also like to thank Dr Tavo Romann for Raman spectroscopy measurements and Al-deposition; Mr Jaan Aruväli for XRD measurements; Marian Külaviir, Hele-Riin Juhkama and Prof. Kalle Kirsimäe for the help with the SEM measurements; Dr Heisi Kurig, Dr Rasmus Palm and Miriam Koppel for gas sorption measurements.

I could not thank enough Ove Korjus, Martin Maide and Alar Heinsaar for keeping the spirit up through all these years. Special thanks to all the people I had the pleasure to share the same 10 m^2 office space, for help and for making the office feel alive. I also want to thank all the colleagues from the chair of physical chemistry for exciting discussions, great ideas and, in general, all the good times.

I would be half the person I am without my loving and supporting family. Dear Riinu and Kaisa, you continue to give my life meaning and purpose when I feel there is none. Thank you!

This research was supported by the EU through the European Regional Development Fund Centers of Excellence, TK141 2014-2020.4.01.15-0011 and TK117 3.2.0101-0030; Estonian Energy Technology Program project 3.2.0501. 10-0015, Material Technology Program project 3.2.1101. 12-0019, Projects of European Structural Funds 3.2.0601.11-0001, 3.2.0304.12-0397; Higher education specialization stipends in smart specialization growth areas 2014-2020.4. 02.16-0026 and Graduate School of Functional materials and technologies in University of Tartu, European Spallation Source: Estonian Participation in ESS Instrument design, development and building and application for scientific research (SLOKT12026T and SLTKT16432T). This work was partially supported by Estonian Research Council Institutional Grant IUT20-13 and IUT20-57, personal research grants PUT55, PUT1033 and PRG 676.

11. PUBLICATIONS

12. CURRICULUM VITAE

Name: Meelis Härmas
Date of birth: March 5, 1990
Citizenship: Estonian
Contact: Institute of Chemistry, University of Tartu
Ravila 14a, 50411, Tartu, Estonia
E-mail: meelis.harmas@ut.ee

Education:

2016–…	University of Tartu – PhD student
2014–2016	University of Tartu – Master's degree in chemistry
2010–2014	University of Tartu – Bachelor's degree in chemistry

Professional Employment:

2014–…	University of Tartu, Institute of Chemistry, Chemist

List of publications:

1. M. Härmas, T. Thomberg, H. Kurig, T. Romann, A. Jänes, E. Lust, Micro-porous–mesoporous carbons for energy storage synthesized by activation of carbonaceous material by zinc chloride, potassium hydroxide or mixture of them, J. Power Sources. 326 (2016) 624–634.
2. M. Härmas, T. Thomberg, T. Romann, A. Jänes, E. Lust, Carbon for Energy Storage Derived from Granulated White Sugar by Hydrothermal Carbonization and Subsequent Zinc Chloride Activation, J. Electrochem. Soc. 164 (2017) A1866–A1872.
3. R. Härmas, R. Palm, M. Härmas, M. Pohl, H. Kurig, I. Tallo, E. Tee, I. Vaas, R. Väli, T. Romann, O. Oll, R. Kanarbik, K. Liivand, J. Eskusson, J. Kruusma, T. Thomberg, A. Jänes, P. Miidla, E. Lust, Influence of porosity parameters and electrolyte chemical composition on the power densities of non-aqueous and ionic liquid based supercapacitors, Electrochimica Acta. 283 (2018) 931–948.
4. J.K. Mathiesen, R. Väli, M. Härmas, E. Lust, J.F.V. Bulow, K.M.Ø. Jensen, P. Norby, Following the In-plane Disorder of Sodiated Hard Carbon through Operando Total Scattering, J. Mater. Chem. A. 7 (2019)
5. R. Väli, J. Aruväli, M. Härmas, A. Jänes, E. Lust, Glycine-Nitrate Process for Synthesis of $Na_3V_2(PO_4)_3$ Cathode Material and Optimization of Glucose-Derived Hard Carbon Anode Material for Characterization in Full Cells, Batteries. 5 (2019) 56.
6. M. Härmas, R. Palm, T. Thomberg, R. Härmas, M. Koppel, M. Paalo, I. Tallo, T. Romann, A. Jänes, E. Lust, Hydrothermal and peat-derived carbons as electrode materials for high-efficient electrical double-layer capacitors, J. Appl. Electrochem. 50 (2020) 15–32.

7. M. Härmas, T. Thomberg, A. Jänes, Effect of Zinc Chloride Activation on D-Glucose Derived Carbons Based Capacitors Performance in Ionic Liquid, J. Electrochem. Soc. 167 (2020) 080533.

13. ELULOOKIRJELDUS

Nimi: Meelis Härmas
Sünniaeg: 5. märts 1990
Kodakondsus: Eesti
Aadress: keemia instituut, Tartu Ülikool,
Ravila 14a, 50411, Tartu, Eesti
E-post: meelis.harmas@ut.ee

Haridustee:

2016–…	Tartu Ülikool – doktorant
2014–2016	Tartu Ülikool – Magistrikraad keemias
2010–2014	Tartu Ülikool – Bakalaureusekraad keemias

Teenistuskäik:

2014–…	Tartu Ülikool, keemia instituut, keemik

Teaduspublikatsioonid:

1. M. Härmas, T. Thomberg, H. Kurig, T. Romann, A. Jänes, E. Lust, Microporous–mesoporous carbons for energy storage synthesized by activation of carbonaceous material by zinc chloride, potassium hydroxide or mixture of them, J. Power Sources. 326 (2016) 624–634.
2. M. Härmas, T. Thomberg, T. Romann, A. Jänes, E. Lust, Carbon for Energy Storage Derived from Granulated White Sugar by Hydrothermal Carbonization and Subsequent Zinc Chloride Activation, J. Electrochem. Soc. 164 (2017) A1866–A1872.
3. R. Härmas, R. Palm, M. Härmas, M. Pohl, H. Kurig, I. Tallo, E. Tee, I. Vaas, R. Väli, T. Romann, O. Oll, R. Kanarbik, K. Liivand, J. Eskusson, J. Kruusma, T. Thomberg, A. Jänes, P. Miidla, E. Lust, Influence of porosity parameters and electrolyte chemical composition on the power densities of non-aqueous and ionic liquid based supercapacitors, Electrochimica Acta. 283 (2018) 931–948.
4. J.K. Mathiesen, R. Väli, M. Härmas, E. Lust, J.F.V. Bulow, K.M.Ø. Jensen, P. Norby, Following the In-plane Disorder of Sodiated Hard Carbon through Operando Total Scattering, J. Mater. Chem. A. 7 (2019) 11709–11717.
5. R. Väli, J. Aruväli, M. Härmas, A. Jänes, E. Lust, Glycine-Nitrate Process for Synthesis of $Na_3V_2(PO_4)_3$ Cathode Material and Optimization of Glucose-Derived Hard Carbon Anode Material for Characterization in Full Cells, Batteries. 5 (2019) 56.
6. M. Härmas, R. Palm, T. Thomberg, R. Härmas, M. Koppel, M. Paalo, I. Tallo, T. Romann, A. Jänes, E. Lust, Hydrothermal and peat-derived carbons as electrode materials for high-efficient electrical double-layer capacitors, J. Appl. Electrochem. 50 (2020) 15–32.

7. M. Härmas, T. Thomberg, A. Jänes, Effect of Zinc Chloride Activation on D-Glucose Derived Carbons Based Capacitors Performance in Ionic Liquid, J. Electrochem. Soc. 167 (2020) 080533.

DISSERTATIONES CHIMICAE UNIVERSITATIS TARTUENSIS

1. **Toomas Tamm.** Quantum-chemical simulation of solvent effects. Tartu, 1993, 110 p.
2. **Peeter Burk.** Theoretical study of gas-phase acid-base equilibria. Tartu, 1994, 96 p.
3. **Victor Lobanov.** Quantitative structure-property relationships in large descriptor spaces. Tartu, 1995, 135 p.
4. **Vahur Mäemets.** The ^{17}O and ^{1}H nuclear magnetic resonance study of H_2O in individual solvents and its charged clusters in aqueous solutions of electrolytes. Tartu, 1997, 140 p.
5. **Andrus Metsala.** Microcanonical rate constant in nonequilibrium distribution of vibrational energy and in restricted intramolecular vibrational energy redistribution on the basis of slater's theory of unimolecular reactions. Tartu, 1997, 150 p.
6. **Uko Maran.** Quantum-mechanical study of potential energy surfaces in different environments. Tartu, 1997, 137 p.
7. **Alar Jänes.** Adsorption of organic compounds on antimony, bismuth and cadmium electrodes. Tartu, 1998, 219 p.
8. **Kaido Tammeveski.** Oxygen electroreduction on thin platinum films and the electrochemical detection of superoxide anion. Tartu, 1998, 139 p.
9. **Ivo Leito.** Studies of Brønsted acid-base equilibria in water and non-aqueous media. Tartu, 1998, 101 p.
10. **Jaan Leis.** Conformational dynamics and equilibria in amides. Tartu, 1998, 131 p.
11. **Toonika Rinken.** The modelling of amperometric biosensors based on oxidoreductases. Tartu, 2000, 108 p.
12. **Dmitri Panov.** Partially solvated Grignard reagents. Tartu, 2000, 64 p.
13. **Kaja Orupõld.** Treatment and analysis of phenolic wastewater with microorganisms. Tartu, 2000, 123 p.
14. **Jüri Ivask.** Ion Chromatographic determination of major anions and cations in polar ice core. Tartu, 2000, 85 p.
15. **Lauri Vares.** Stereoselective Synthesis of Tetrahydrofuran and Tetrahydropyran Derivatives by Use of Asymmetric Horner-Wadsworth-Emmons and Ring Closure Reactions. Tartu, 2000, 184 p.
16. **Martin Lepiku.** Kinetic aspects of dopamine D_2 receptor interactions with specific ligands. Tartu, 2000, 81 p.
17. **Katrin Sak.** Some aspects of ligand specificity of P2Y receptors. Tartu, 2000, 106 p.
18. **Vello Pällin.** The role of solvation in the formation of iotsitch complexes. Tartu, 2001, 95 p.
19. **Katrin Kollist.** Interactions between polycyclic aromatic compounds and humic substances. Tartu, 2001, 93 p.

20. **Ivar Koppel.** Quantum chemical study of acidity of strong and superstrong Brønsted acids. Tartu, 2001, 104 p.
21. **Viljar Pihl.** The study of the substituent and solvent effects on the acidity of OH and CH acids. Tartu, 2001, 132 p.
22. **Natalia Palm.** Specification of the minimum, sufficient and significant set of descriptors for general description of solvent effects. Tartu, 2001, 134 p.
23. **Sulev Sild.** QSPR/QSAR approaches for complex molecular systems. Tartu, 2001, 134 p.
24. **Ruslan Petrukhin.** Industrial applications of the quantitative structure-property relationships. Tartu, 2001, 162 p.
25. **Boris V. Rogovoy.** Synthesis of (benzotriazolyl)carboximidamides and their application in relations with *N*- and *S*-nucleophyles. Tartu, 2002, 84 p.
26. **Koit Herodes.** Solvent effects on UV-vis absorption spectra of some solvatochromic substances in binary solvent mixtures: the preferential solvation model. Tartu, 2002, 102 p.
27. **Anti Perkson.** Synthesis and characterisation of nanostructured carbon. Tartu, 2002, 152 p.
28. **Ivari Kaljurand.** Self-consistent acidity scales of neutral and cationic Brønsted acids in acetonitrile and tetrahydrofuran. Tartu, 2003, 108 p.
29. **Karmen Lust.** Adsorption of anions on bismuth single crystal electrodes. Tartu, 2003, 128 p.
30. **Mare Piirsalu.** Substituent, temperature and solvent effects on the alkaline hydrolysis of substituted phenyl and alkyl esters of benzoic acid. Tartu, 2003, 156 p.
31. **Meeri Sassian.** Reactions of partially solvated Grignard reagents. Tartu, 2003, 78 p.
32. **Tarmo Tamm.** Quantum chemical modelling of polypyrrole. Tartu, 2003. 100 p.
33. **Erik Teinemaa.** The environmental fate of the particulate matter and organic pollutants from an oil shale power plant. Tartu, 2003. 102 p.
34. **Jaana Tammiku-Taul.** Quantum chemical study of the properties of Grignard reagents. Tartu, 2003. 120 p.
35. **Andre Lomaka.** Biomedical applications of predictive computational chemistry. Tartu, 2003. 132 p.
36. **Kostyantyn Kirichenko.** Benzotriazole – Mediated Carbon–Carbon Bond Formation. Tartu, 2003. 132 p.
37. **Gunnar Nurk.** Adsorption kinetics of some organic compounds on bismuth single crystal electrodes. Tartu, 2003, 170 p.
38. **Mati Arulepp.** Electrochemical characteristics of porous carbon materials and electrical double layer capacitors. Tartu, 2003, 196 p.
39. **Dan Cornel Fara.** QSPR modeling of complexation and distribution of organic compounds. Tartu, 2004, 126 p.
40. **Riina Mahlapuu.** Signalling of galanin and amyloid precursor protein through adenylate cyclase. Tartu, 2004, 124 p.

41. **Mihkel Kerikmäe.** Some luminescent materials for dosimetric applications and physical research. Tartu, 2004, 143 p.
42. **Jaanus Kruusma.** Determination of some important trace metal ions in human blood. Tartu, 2004, 115 p.
43. **Urmas Johanson.** Investigations of the electrochemical properties of polypyrrole modified electrodes. Tartu, 2004, 91 p.
44. **Kaido Sillar.** Computational study of the acid sites in zeolite ZSM-5. Tartu, 2004, 80 p.
45. **Aldo Oras.** Kinetic aspects of dATPαS interaction with $P2Y_1$ receptor. Tartu, 2004, 75 p.
46. **Erik Mölder.** Measurement of the oxygen mass transfer through the air-water interface. Tartu, 2005, 73 p.
47. **Thomas Thomberg.** The kinetics of electroreduction of peroxodisulfate anion on cadmium (0001) single crystal electrode. Tartu, 2005, 95 p.
48. **Olavi Loog.** Aspects of condensations of carbonyl compounds and their imine analogues. Tartu, 2005, 83 p.
49. **Siim Salmar.** Effect of ultrasound on ester hydrolysis in aqueous ethanol. Tartu, 2006, 73 p.
50. **Ain Uustare.** Modulation of signal transduction of heptahelical receptors by other receptors and G proteins. Tartu, 2006, 121 p.
51. **Sergei Yurchenko.** Determination of some carcinogenic contaminants in food. Tartu, 2006, 143 p.
52. **Kaido Tämm.** QSPR modeling of some properties of organic compounds. Tartu, 2006, 67 p.
53. **Olga Tšubrik.** New methods in the synthesis of multisubstituted hydrazines. Tartu. 2006, 183 p.
54. **Lilli Sooväli.** Spectrophotometric measurements and their uncertainty in chemical analysis and dissociation constant measurements. Tartu, 2006, 125 p.
55. **Eve Koort.** Uncertainty estimation of potentiometrically measured ph and pK_a values. Tartu, 2006, 139 p.
56. **Sergei Kopanchuk.** Regulation of ligand binding to melanocortin receptor subtypes. Tartu, 2006, 119 p.
57. **Silvar Kallip.** Surface structure of some bismuth and antimony single crystal electrodes. Tartu, 2006, 107 p.
58. **Kristjan Saal.** Surface silanization and its application in biomolecule coupling. Tartu, 2006, 77 p.
59. **Tanel Tätte.** High viscosity $Sn(OBu)_4$ oligomeric concentrates and their applications in technology. Tartu, 2006, 91 p.
60. **Dimitar Atanasov Dobchev**. Robust QSAR methods for the prediction of properties from molecular structure. Tartu, 2006, 118 p.
61. **Hannes Hagu**. Impact of ultrasound on hydrophobic interactions in solutions. Tartu, 2007, 81 p.
62. **Rutha Jäger.** Electroreduction of peroxodisulfate anion on bismuth electrodes. Tartu, 2007, 142 p.

63. **Kaido Viht.** Immobilizable bisubstrate-analogue inhibitors of basophilic protein kinases: development and application in biosensors. Tartu, 2007, 88 p.
64. **Eva-Ingrid Rõõm.** Acid-base equilibria in nonpolar media. Tartu, 2007, 156 p.
65. **Sven Tamp.** DFT study of the cesium cation containing complexes relevant to the cesium cation binding by the humic acids. Tartu, 2007, 102 p.
66. **Jaak Nerut.** Electroreduction of hexacyanoferrate(III) anion on Cadmium (0001) single crystal electrode. Tartu, 2007, 180 p.
67. **Lauri Jalukse.** Measurement uncertainty estimation in amperometric dissolved oxygen concentration measurement. Tartu, 2007, 112 p.
68. **Aime Lust.** Charge state of dopants and ordered clusters formation in CaF_2:Mn and CaF_2:Eu luminophors. Tartu, 2007, 100 p.
69. **Iiris Kahn**. Quantitative Structure-Activity Relationships of environmentally relevant properties. Tartu, 2007, 98 p.
70. **Mari Reinik.** Nitrates, nitrites, N-nitrosamines and polycyclic aromatic hydrocarbons in food: analytical methods, occurrence and dietary intake. Tartu, 2007, 172 p.
71. **Heili Kasuk.** Thermodynamic parameters and adsorption kinetics of organic compounds forming the compact adsorption layer at Bi single crystal electrodes. Tartu, 2007, 212 p.
72. **Erki Enkvist.** Synthesis of adenosine-peptide conjugates for biological applications. Tartu, 2007, 114 p.
73. **Svetoslav Hristov Slavov**. Biomedical applications of the QSAR approach. Tartu, 2007, 146 p.
74. **Eneli Härk.** Electroreduction of complex cations on electrochemically polished Bi(*hkl*) single crystal electrodes. Tartu, 2008, 158 p.
75. **Priit Möller.** Electrochemical characteristics of some cathodes for medium temperature solid oxide fuel cells, synthesized by solid state reaction technique. Tartu, 2008, 90 p.
76. **Signe Viggor.** Impact of biochemical parameters of genetically different pseudomonads at the degradation of phenolic compounds. Tartu, 2008, 122 p.
77. **Ave Sarapuu.** Electrochemical reduction of oxygen on quinone-modified carbon electrodes and on thin films of platinum and gold. Tartu, 2008, 134 p.
78. **Agnes Kütt.** Studies of acid-base equilibria in non-aqueous media. Tartu, 2008, 198 p.
79. **Rouvim Kadis.** Evaluation of measurement uncertainty in analytical chemistry: related concepts and some points of misinterpretation. Tartu, 2008, 118 p.
80. **Valter Reedo.** Elaboration of IVB group metal oxide structures and their possible applications. Tartu, 2008, 98 p.
81. **Aleksei Kuznetsov.** Allosteric effects in reactions catalyzed by the cAMP-dependent protein kinase catalytic subunit. Tartu, 2009, 133 p.

82. **Aleksei Bredihhin.** Use of mono- and polyanions in the synthesis of multisubstituted hydrazine derivatives. Tartu, 2009, 105 p.
83. **Anu Ploom.** Quantitative structure-reactivity analysis in organosilicon chemistry. Tartu, 2009, 99 p.
84. **Argo Vonk.** Determination of adenosine A_{2A}- and dopamine D_1 receptor-specific modulation of adenylate cyclase activity in rat striatum. Tartu, 2009, 129 p.
85. **Indrek Kivi.** Synthesis and electrochemical characterization of porous cathode materials for intermediate temperature solid oxide fuel cells. Tartu, 2009, 177 p.
86. **Jaanus Eskusson.** Synthesis and characterisation of diamond-like carbon thin films prepared by pulsed laser deposition method. Tartu, 2009, 117 p.
87. **Marko Lätt.** Carbide derived microporous carbon and electrical double layer capacitors. Tartu, 2009, 107 p.
88. **Vladimir Stepanov.** Slow conformational changes in dopamine transporter interaction with its ligands. Tartu, 2009, 103 p.
89. **Aleksander Trummal.** Computational Study of Structural and Solvent Effects on Acidities of Some Brønsted Acids. Tartu, 2009, 103 p.
90. **Eerold Vellemäe.** Applications of mischmetal in organic synthesis. Tartu, 2009, 93 p.
91. **Sven Parkel.** Ligand binding to 5-HT_{1A} receptors and its regulation by Mg^{2+} and Mn^{2+}. Tartu, 2010, 99 p.
92. **Signe Vahur.** Expanding the possibilities of ATR-FT-IR spectroscopy in determination of inorganic pigments. Tartu, 2010, 184 p.
93. **Tavo Romann**. Preparation and surface modification of bismuth thin film, porous, and microelectrodes. Tartu, 2010, 155 p.
94. **Nadežda Aleksejeva.** Electrocatalytic reduction of oxygen on carbon nanotube-based nanocomposite materials. Tartu, 2010, 147 p.
95. **Marko Kullapere.** Electrochemical properties of glassy carbon, nickel and gold electrodes modified with aryl groups. Tartu, 2010, 233 p.
96. **Liis Siinor.** Adsorption kinetics of ions at Bi single crystal planes from aqueous electrolyte solutions and room-temperature ionic liquids. Tartu, 2010, 101 p.
97. **Angela Vaasa.** Development of fluorescence-based kinetic and binding assays for characterization of protein kinases and their inhibitors. Tartu 2010, 101 p.
98. **Indrek Tulp.** Multivariate analysis of chemical and biological properties. Tartu 2010, 105 p.
99. **Aare Selberg.** Evaluation of environmental quality in Northern Estonia by the analysis of leachate. Tartu 2010, 117 p.
100. **Darja Lavõgina.** Development of protein kinase inhibitors based on adenosine analogue-oligoarginine conjugates. Tartu 2010, 248 p.
101. **Laura Herm.** Biochemistry of dopamine D_2 receptors and its association with motivated behaviour. Tartu 2010, 156 p.

102. **Terje Raudsepp.** Influence of dopant anions on the electrochemical properties of polypyrrole films. Tartu 2010, 112 p.
103. **Margus Marandi.** Electroformation of Polypyrrole Films: *In-situ* AFM and STM Study. Tartu 2011, 116 p.
104. **Kairi Kivirand.** Diamine oxidase-based biosensors: construction and working principles. Tartu, 2011, 140 p.
105. **Anneli Kruve.** Matrix effects in liquid-chromatography electrospray mass-spectrometry. Tartu, 2011, 156 p.
106. **Gary Urb.** Assessment of environmental impact of oil shale fly ash from PF and CFB combustion. Tartu, 2011, 108 p.
107. **Nikita Oskolkov.** A novel strategy for peptide-mediated cellular delivery and induction of endosomal escape. Tartu, 2011, 106 p.
108. **Dana Martin.** The QSPR/QSAR approach for the prediction of properties of fullerene derivatives. Tartu, 2011, 98 p.
109. **Säde Viirlaid.** Novel glutathione analogues and their antioxidant activity. Tartu, 2011, 106 p.
110. **Ülis Sõukand.** Simultaneous adsorption of Cd^{2+}, Ni^{2+}, and Pb^{2+} on peat. Tartu, 2011, 124 p.
111. **Lauri Lipping.** The acidity of strong and superstrong Brønsted acids, an outreach for the "limits of growth": a quantum chemical study. Tartu, 2011, 124 p.
112. **Heisi Kurig.** Electrical double-layer capacitors based on ionic liquids as electrolytes. Tartu, 2011, 146 p.
113. **Marje Kasari.** Bisubstrate luminescent probes, optical sensors and affinity adsorbents for measurement of active protein kinases in biological samples. Tartu, 2012, 126 p.
114. **Kalev Takkis.** Virtual screening of chemical databases for bioactive molecules. Tartu, 2012, 122 p.
115. **Ksenija Kisseljova**. Synthesis of aza-β^3-amino acid containing peptides and kinetic study of their phosphorylation by protein kinase A. Tartu, 2012, 104 p.
116. **Riin Rebane.** Advanced method development strategy for derivatization LC/ESI/MS. Tartu, 2012, 184 p.
117. **Vladislav Ivaništšev.** Double layer structure and adsorption kinetics of ions at metal electrodes in room temperature ionic liquids. Tartu, 2012, 128 p.
118. **Irja Helm.** High accuracy gravimetric Winkler method for determination of dissolved oxygen. Tartu, 2012, 139 p.
119. **Karin Kipper.** Fluoroalcohols as Components of LC-ESI-MS Eluents: Usage and Applications. Tartu, 2012, 164 p.
120. **Arno Ratas.** Energy storage and transfer in dosimetric luminescent materials. Tartu, 2012, 163 p.
121. **Reet Reinart-Okugbeni**. Assay systems for characterisation of subtype-selective binding and functional activity of ligands on dopamine receptors. Tartu, 2012, 159 p.

122. **Lauri Sikk.** Computational study of the Sonogashira cross-coupling reaction. Tartu, 2012, 81 p.
123. **Karita Raudkivi.** Neurochemical studies on inter-individual differences in affect-related behaviour of the laboratory rat. Tartu, 2012, 161 p.
124. **Indrek Saar.** Design of GalR2 subtype specific ligands: their role in depression-like behavior and feeding regulation. Tartu, 2013, 126 p.
125. **Ann Laheäär.** Electrochemical characterization of alkali metal salt based non-aqueous electrolytes for supercapacitors. Tartu, 2013, 127 p.
126. **Kerli Tõnurist.** Influence of electrospun separator materials properties on electrochemical performance of electrical double-layer capacitors. Tartu, 2013, 147 p.
127. **Kaija Põhako-Esko.** Novel organic and inorganic ionogels: preparation and characterization. Tartu, 2013, 124 p.
128. **Ivar Kruusenberg.** Electroreduction of oxygen on carbon nanomaterial-based catalysts. Tartu, 2013, 191 p.
129. **Sander Piiskop.** Kinetic effects of ultrasound in aqueous acetonitrile solutions. Tartu, 2013, 95 p.
130. **Ilona Faustova**. Regulatory role of L-type pyruvate kinase N-terminal domain. Tartu, 2013, 109 p.
131. **Kadi Tamm.** Synthesis and characterization of the micro-mesoporous anode materials and testing of the medium temperature solid oxide fuel cell single cells. Tartu, 2013, 138 p.
132. **Iva Bozhidarova Stoyanova-Slavova.** Validation of QSAR/QSPR for regulatory purposes. Tartu, 2013, 109 p.
133. **Vitali Grozovski**. Adsorption of organic molecules at single crystal electrodes studied by *in situ* STM method. Tartu, 2014, 146 p.
134. **Santa Veikšina**. Development of assay systems for characterisation of ligand binding properties to melanocortin 4 receptors. Tartu, 2014, 151 p.
135. **Jüri Liiv.** PVDF (polyvinylidene difluoride) as material for active element of twisting-ball displays. Tartu, 2014, 111 p.
136. **Kersti Vaarmets.** Electrochemical and physical characterization of pristine and activated molybdenum carbide-derived carbon electrodes for the oxygen electroreduction reaction. Tartu, 2014, 131 p.
137. **Lauri Tõntson**. Regulation of G-protein subtypes by receptors, guanine nucleotides and Mn^{2+}. Tartu, 2014, 105 p.
138. **Aiko Adamson.** Properties of amine-boranes and phosphorus analogues in the gas phase. Tartu, 2014, 78 p.
139. **Elo Kibena**. Electrochemical grafting of glassy carbon, gold, highly oriented pyrolytic graphite and chemical vapour deposition-grown graphene electrodes by diazonium reduction method. Tartu, 2014, 184 p.
140. **Teemu Näykki.** Novel Tools for Water Quality Monitoring – From Field to Laboratory. Tartu, 2014, 202 p.
141. **Karl Kaupmees.** Acidity and basicity in non-aqueous media: importance of solvent properties and purity. Tartu, 2014, 128 p.

142. **Oleg Lebedev**. Hydrazine polyanions: different strategies in the synthesis of heterocycles. Tartu, 2015, 118 p.
143. **Geven Piir.** Environmental risk assessment of chemicals using QSAR methods. Tartu, 2015, 123 p.
144. **Olga Mazina.** Development and application of the biosensor assay for measurements of cyclic adenosine monophosphate in studies of G protein-coupled receptor signalinga. Tartu, 2015, 116 p.
145. **Sandip Ashokrao Kadam.** Anion receptors: synthesis and accurate binding measurements. Tartu, 2015, 116 p.
146. **Indrek Tallo.** Synthesis and characterization of new micro-mesoporous carbide derived carbon materials for high energy and power density electrical double layer capacitors. Tartu, 2015, 148 p.
147. **Heiki Erikson.** Electrochemical reduction of oxygen on nanostructured palladium and gold catalysts. Tartu, 2015, 204 p.
148. **Erik Anderson.** *In situ* Scanning Tunnelling Microscopy studies of the interfacial structure between Bi(111) electrode and a room temperature ionic liquid. Tartu, 2015, 118 p.
149. **Girinath G. Pillai.** Computational Modelling of Diverse Chemical, Biochemical and Biomedical Properties. Tartu, 2015, 140 p.
150. **Piret Pikma.** Interfacial structure and adsorption of organic compounds at Cd(0001) and Sb(111) electrodes from ionic liquid and aqueous electrolytes: an *in situ* STM study. Tartu, 2015, 126 p.
151. **Ganesh babu Manoharan.** Combining chemical and genetic approaches for photoluminescence assays of protein kinases. Tartu, 2016, 126 p.
152. **Carolin Siimenson**. Electrochemical characterization of halide ion adsorption from liquid mixtures at Bi(111) and pyrolytic graphite electrode surface. Tartu, 2016, 110 p.
153. **Asko Laaniste.** Comparison and optimisation of novel mass spectrometry ionisation sources. Tartu, 2016, 156 p.
154. **Hanno Evard.** Estimating limit of detection for mass spectrometric analysis methods. Tartu, 2016, 224 p.
155. **Kadri Ligi.** Characterization and application of protein kinase-responsive organic probes with triplet-singlet energy transfer. Tartu, 2016, 122 p.
156. **Margarita Kagan.** Biosensing penicillins' residues in milk flows. Tartu, 2016, 130 p.
157. **Marie Kriisa.** Development of protein kinase-responsive photoluminescent probes and cellular regulators of protein phosphorylation. Tartu, 2016, 106 p.
158. **Mihkel Vestli.** Ultrasonic spray pyrolysis deposited electrolyte layers for intermediate temperature solid oxide fuel cells. Tartu, 2016, 156 p.
159. **Silver Sepp**. Influence of porosity of the carbide-derived carbon on the properties of the composite electrocatalysts and characteristics of polymer electrolyte fuel cells. Tartu, 2016, 137 p.
160. **Kristjan Haav**. Quantitative relative equilibrium constant measurements in supramolecular chemistry. Tartu, 2017, 158 p.

161. **Anu Teearu**. Development of MALDI-FT-ICR-MS methodology for the analysis of resinous materials. Tartu, 2017, 205 p.
162. **Taavi Ivan**. Bifunctional inhibitors and photoluminescent probes for studies on protein complexes. Tartu, 2017, 140 p.
163. **Maarja-Liisa Oldekop**. Characterization of amino acid derivatization reagents for LC-MS analysis. Tartu, 2017, 147 p.
164. **Kristel Jukk**. Electrochemical reduction of oxygen on platinum- and palladium-based nanocatalysts. Tartu, 2017, 250 p.
165. **Siim Kukk**. Kinetic aspects of interaction between dopamine transporter and *N*-substituted nortropane derivatives. Tartu, 2017, 107 p.
166. **Birgit Viira**. Design and modelling in early drug development in targeting HIV-1 reverse transcriptase and Malaria. Tartu, 2017, 172 p.
167. **Rait Kivi**. Allostery in cAMP dependent protein kinase catalytic subunit. Tartu, 2017, 115 p.
168. **Agnes Heering**. Experimental realization and applications of the unified acidity scale. Tartu, 2017, 123 p.
169. **Delia Juronen**. Biosensing system for the rapid multiplex detection of mastitis-causing pathogens in milk. Tartu, 2018, 85 p.
170. **Hedi Rahnel.** ARC-inhibitors: from reliable biochemical assays to regulators of physiology of cells. Tartu, 2018, 176 p.
171. **Anton Ruzanov.** Computational investigation of the electrical double layer at metal–aqueous solution and metal–ionic liquid interfaces. Tartu, 2018, 129 p.
172. **Katrin Kestav.** Crystal Structure-Guided Development of Bisubstrate-Analogue Inhibitors of Mitotic Protein Kinase Haspin. Tartu, 2018, 166 p.
173. **Mihkel Ilisson.** Synthesis of novel heterocyclic hydrazine derivatives and their conjugates. Tartu, 2018, 101 p.
174. **Anni Allikalt.** Development of assay systems for studying ligand binding to dopamine receptors. Tartu, 2018, 160 p.
175. **Ove Oll.** Electrical double layer structure and energy storage characteristics of ionic liquid based capacitors. Tartu, 2018, 187 p.
176. **Rasmus Palm.** Carbon materials for energy storage applications. Tartu, 2018, 114 p.
177. **Jörgen Metsik.** Preparation and stability of poly(3,4-ethylenedioxythiophene) thin films for transparent electrode applications. Tartu, 2018, 111 p.
178. **Sofja Tšepelevitš.** Experimental studies and modeling of solute-solvent interactions. Tartu, 2018, 109 p.
179. **Märt Lõkov.** Basicity of some nitrogen, phosphorus and carbon bases in acetonitrile. Tartu, 2018, 104 p.
180. **Anton Mastitski**. Preparation of α-aza-amino acid precursors and related compounds by novel methods of reductive one-pot alkylation and direct alkylation. Tartu, 2018, 155 p.
181. **Jürgen Vahter**. Development of bisubstrate inhibitors for protein kinase CK2. Tartu, 2019, 186 p.

182. **Piia Liigand.** Expanding and improving methodology and applications of ionization efficiency measurements. Tartu, 2019, 189 p.
183. **Sigrid Selberg.** Synthesis and properties of lipophilic phosphazene-based indicator molecules. Tartu, 2019, 74 p.
184. **Jaanus Liigand.** Standard substance free quantification for LC/ESI/MS analysis based on the predicted ionization efficiencies. Tartu, 2019, 254 p.
185. **Marek Mooste.** Surface and electrochemical characterisation of aryl film and nanocomposite material modified carbon and metal-based electrodes. Tartu, 2019, 304 p.
186. **Mare Oja.** Experimental investigation and modelling of pH profiles for effective membrane permeability of drug substances. Tartu, 2019, 306 p.
187. **Sajid Hussain.** Electrochemical reduction of oxygen on supported Pt catalysts. Tartu, 2019, 220 p.
188. **Ronald Väli.** Glucose-derived hard carbon electrode materials for sodium-ion batteries. Tartu, 2019, 180 p.
189. **Ester Tee.** Analysis and development of selective synthesis methods of hierarchical micro- and mesoporous carbons. Tartu, 2019, 210 p.
190. **Martin Maide.** Influence of the microstructure and chemical composition of the fuel electrode on the electrochemical performance of reversible solid oxide fuel cell. Tartu, 2020, 144 p.
191. **Edith Viirlaid.** Biosensing Pesticides in Water Samples. Tartu, 2020, 102 p.
192. **Maike Käärik.** Nanoporous carbon: the controlled nanostructure, and structure-property relationships. Tartu, 2020, 162 p.
193. **Artur Gornischeff.** Study of ionization efficiencies for derivatized compounds in LC/ESI/MS and their application for targeted analysis. Tartu, 2020, 124 p.
194. **Reet Link.** Ligand binding, allosteric modulation and constitutive activity of melanocortin-4 receptors. Tartu, 2020, 108 p.
195. **Pilleriin Peets.** Development of instrumental methods for the analysis of textile fibres and dyes. Tartu, 2020, 150 p.
196. **Larisa Ivanova.** Design of active compounds against neurodegenerative diseases. Tartu, 2020, 152 p.